Harmonic State-Space Modeling and System Characteristic Analysis of Grid-Connected Inverter Parallel-Operation System Considering Asynchronous Carriers

Yuxi Cai, *Student Member, IEEE*, Yingjie He, *Senior Member, IEEE*, Haoting Du, *Student Member, IEEE*, and Jinjun Liu, *Fellow, IEEE*

***Abstract*—In *LCL* grid-connected inverter, low switching frequency makes the control loop, filter resonant peak, and sideband harmonics generated by modulation coupled in mid-frequency band. When multiple inverters operate in parallel, the asynchronous carrier phase (i.e., asynchronous carriers) will cause additional mid-frequency resonance in each inverter. This will coexist with the inherent mid-frequency harmonic coupling of each inverter. Then, the mid-frequency harmonic characteristics of parallel system will become more complex, which will increase the difficulty of accurately modeling, and analyzing the harmonic characteristics of the output current of each inverter and total grid-connected current. Based on this, a complete harmonic state-space (HSS) model of parallel system considering asynchronous carriers and its frequency-domain analysis method are proposed in this article, which realizes the accurate analysis of the impact of asynchronous carriers on system harmonic characteristics. Meanwhile, an iterative calculation method of parallel-system HSS model considering asynchronous carriers is proposed, which realizes the efficient and accurate calculation of the output current harmonic amplitude and phase of each inverter. Finally, the effectiveness of the proposed model and analysis method are verified through simulations and experiments.**

***Index Terms*—Asynchronous carriers, harmonic characteristic analysis, harmonic state-space (HSS), *LCL* grid-connected inverter (*LCL* GCI), low switching frequency (LSF), parallel operation.**

I. Introduction

In RECENT years, the new energy power generation system represented by photovoltaic and wind power is an important industry with rapid development in the world, and has gradually become the research hotspot in the field of power electronics [1], [2], [3]. Among them, the *LCL* grid-connected inverter (GCI) is the core device in the new energy generation system and the interface between the new energy generation device and the utility grid. Its accurate modeling is an important prerequisite for the analysis of system harmonic characteristics and harmonic calculation [4].

When *LCL* GCIs operate in parallel (as shown in Fig. 1), it is a common phenomenon that the carrier phase of each inverter is not synchronized (i.e., asynchronous carriers) [5]. Asynchronous carriers will cause the inconsistency of the instantaneous switching sequence of the power devices in each inverter, which will lead to the energy interaction between each inverter [6], [7]. This will eventually lead to additional resonance between inverters operating in parallel compared to a single inverter operating independently [8]. In mid-frequency band, due to the existence of the resonant peak of *LCL* filter, the equivalent output impedance of GCI is smaller than that in low- and high-frequency bands [9], [10]. Therefore, when multiple GCIs operate in parallel, the resonance phenomenon caused by asynchronous carriers in each inverter mainly exists near the resonant point of inverter, that is, the asynchronous carriers will cause additional mid-frequency resonance in each inverter [11].

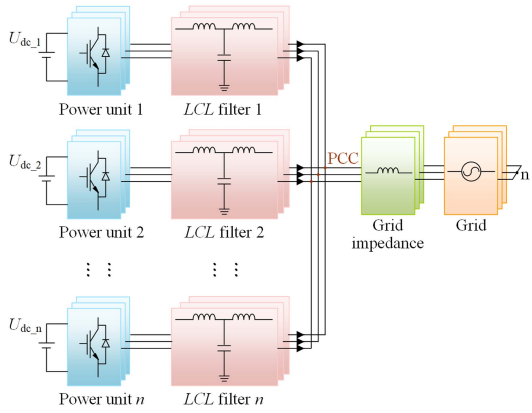

Fig. 1. Schematic diagram of parallel operation of multiple inverters.

Manuscript received 15 September 2023; revised 11 January 2024; accepted 13 March 2024. Date of publication 27 March 2024; date of current version 16 May 2024. This work was supported in part by the Aeronautical Science Foundation of China under Grant 20230040070017, in part by the Natural Science Foundation of Shaanxi Province under Grant 2023-JC-YB-367, in part by "Chunhui Plan" Cooperative Research Project of the Education Ministry under Grant 202200765, and in part by the "Qinchuangyuan Scientist + Engineer" Program of Shaanxi Province under Grant 2024QCY-KXJ-138. Recommended for publication by Associate Editor K. Gunawardane. *(Corresponding author: Yingjie He.)*

Yuxi Cai is with the School of Electrical Engineering, Xi'an Jiaotong University, Xi'an 710049, China, and also with the Xi'an Research Institute of High-Tech, Xi'an 710025, China (e-mail: 412561351@163.com).

Yingjie He, Haoting Du, and Jinjun Liu are with the School of Electrical Engineering, Xi'an Jiaotong University, Xi'an 710049, China (e-mail: hyj202411@sina.com; tommydht@stu.xjtu.edu.cn; jjliu@mail.xjtu.edu.cn).

Color versions of one or more figures in this article are available at https://doi.org/10.1109/TPEL.2024.3381813.

Digital Object Identifier 10.1109/TPEL.2024.3381813

According to the relevant research on low switching frequency (LSF) *LCL* GCI, the control loop, filter resonant peak and sideband harmonics generated by modulation have inherent mid-frequency harmonic coupling [12], [13]. Therefore, when inverters operate in parallel, the mid-frequency resonance generated by asynchronous carriers will coexist with the inherent mid-frequency harmonic coupling of each inverter. This makes the harmonic characteristics of each inverter more complicated, and further increases the difficulty of analyzing the harmonic characteristics of the output current of each inverter and total grid-connected current [8]. Here, the mid-frequency resonance generated by asynchronous carriers is not only related to the instantaneous switching state, modulation, filter parameters of each inverter, but also to the control system parameters. Thus, in order to accurately and comprehensively analyze the harmonic characteristics and stability for parallel system of LSF *LCL* GCI, it is necessary to construct an accurate mathematical model for parallel system that can reflect its harmonic characteristics in detail.

For the parallel system shown in Fig. 1, the most commonly used modeling methods are single-frequency-based impedance modeling method and state-space averaging (SSAV) modeling method. The impedance modeling method regards the inverter as a "black box" and models the output voltage and current at its ports [14], [15], [16], [17]. The impedance model is more commonly used to analyze the external characteristics of the system and is difficult to reflect the internal harmonic characteristics of the system [18], [19]. In the SSAV model of parallel system, the state-space matrix of parallel system is formed by merging the state-space matrices of multiple inverters [20], [21], [22]. This model can perform disturbance analysis on circulating, harmonics, and power fluctuations [23], [24], and can roughly reflect the internal and output characteristics of each inverter. It is suitable for simple analysis of resonance phenomena in the system [25]. However, in the LSF inverter parallel system, each single inverter has both inherent mid-frequency harmonic coupling and mid-frequency resonance caused by asynchronous carriers, which makes the mid-frequency harmonic characteristics of each inverter more complex, the single-frequency-based impedance model and SSAV model are no longer applicable. It is necessary to use the multifrequency model to analyze the harmonic characteristics of the LSF parallel system in detail [26], [27]. The work in [28] and [29] regarded the asynchronous carriers as a disturbance, built a generalized averaging model of the modulation unit, and analyzed the influence of the asynchronous carriers on the sideband harmonics of a single inverter. The premise of this research is that the frequency of the mid-frequency resonance caused by asynchronous carriers is known. However, it is difficult to obtain this resonance frequency, and these articles do not explain its acquisition method. Another multifrequency modeling method is the harmonic state-space (HSS) modeling method. It can reflect the relationship between each input harmonic component and each output harmonic component in the system [30], [31], [32]. At present, there have been some research results on the application of HSS to *LCL* inverter [33], [34]. Thus, extending the HSS modeling method of the single inverter to the parallel system is a feasible method for detailed analysis of the output harmonic characteristics and stability of each inverter under asynchronous carriers [8]. Kwon et al. [35] established the HSS model of inverter parallel system including the cable model, and realized the stability analysis of the parallel system with multiple operating points. This article drew the Jacobian sparse matrix diagram of the parallel system with five inverters, which intuitively reflected how the grid voltage harmonics are coupled with the output current harmonics through the harmonic impedance. However, this article fails to consider the asynchronous carrier problem when multiple inverters are connected in parallel, so the HSS model of the parallel system established is still inaccurate and needs to be improved. At present, there are few reports on the research on HSS modeling and analysis of inverter parallel system, which is still in the initial stage, and related theoretical research needs to be developed and improved.

Based on the current research status and shortcomings, this article takes the parallel system of two LSF *LCL* GCIs as an example, based on the research on single-inverter HSS modeling and harmonic calculation method completed by our team [12], [13], the extension methods of their application to inverter parallel system with asynchronous carriers are studied.

The contributions and practical significance of this article are as follows.

1) A complete HSS model and frequency-domain analysis method for parallel system considering asynchronous carriers are proposed. They effectively improve the accuracy of harmonic stability analysis for parallel system, and are of great significance for evaluating system characteristics and guiding system parameter optimization design.
2) An HSS-model iterative calculation method for parallel system considering asynchronous carriers is proposed, which realizes the efficient and accurate calculation of the amplitude and phase of each-inverter output-current harmonics and total grid-connected current harmonics. It can replace the circuit simulation, and is fully implemented in code form, with strong flexibility and portability.

The rest of this article is organized as follows. Section II describes the structure of the *LCL* GCI parallel system. In Section III, the construction method of the complete HSS model suitable for frequency-domain analysis, and the iterative calculation method of the HSS model are extended to the parallel system considering asynchronous carriers. In Section IV, based on the complete HSS model of parallel system, the system characteristics are comprehensively analyzed in frequency domain, and the impact of asynchronous carriers on harmonic characteristics is studied. Section V verifies the accuracy of the iterative calculation method for parallel-system HSS model. In Section VI, the effectiveness and correctness of the established model and harmonic analysis method are verified through experiments. Section VII is the discussion on the extension of proposed methods in parallel system of n inverters. Section VIII concludes this article.

II. System Structure

Fig. 2 shows the parallel operation system of two neutral-point-clamped three-level *LCL* GCIs. Among them, $C_{\mathrm{dc}\,q1}$ and $C_{\mathrm{dc}\,q2}$ $(q=1,2)$ are the two dc-side capacitors of the qth inverter,

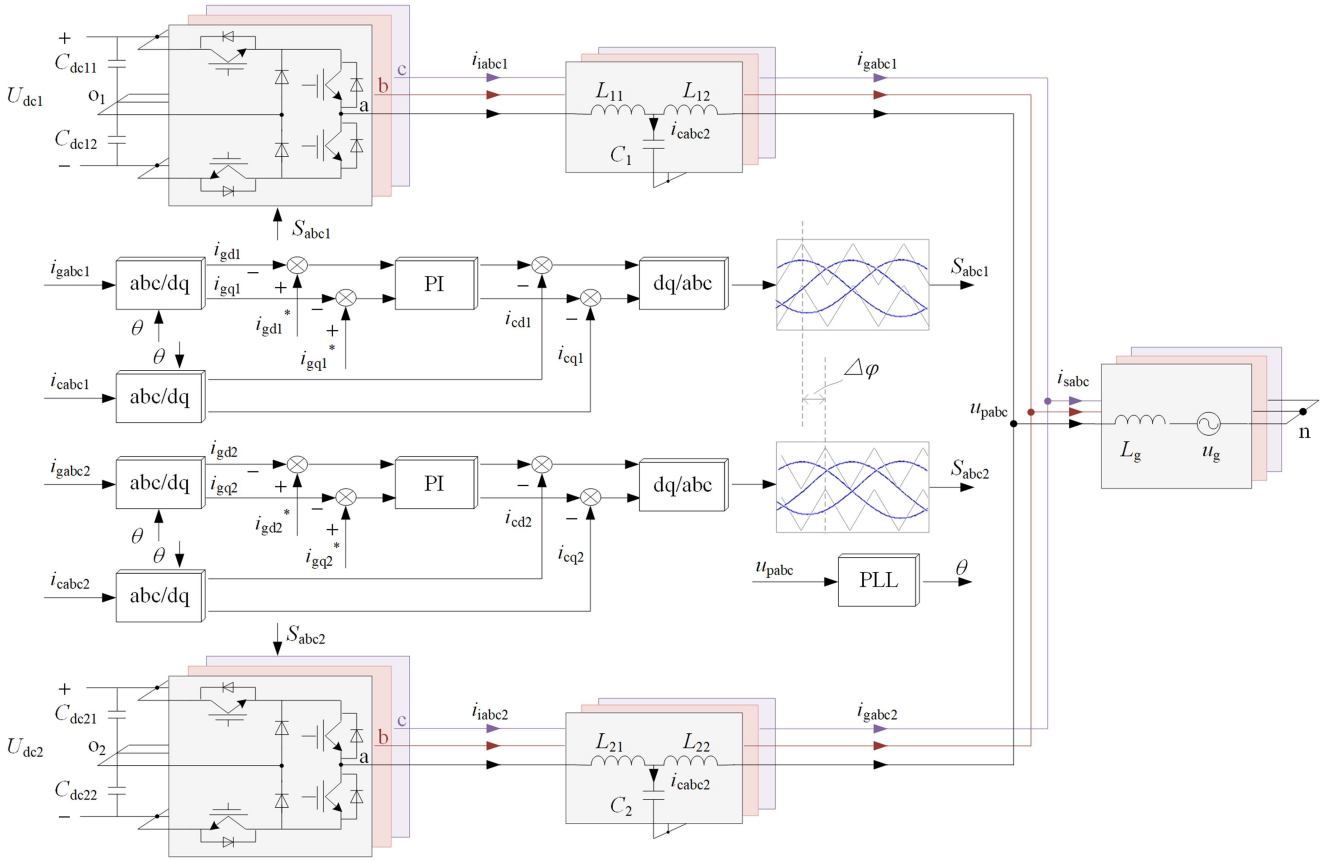

Fig. 2. Parallel operation system of two *LCL* GCIs.

respectively; L_{q1}, L_{q2}, and C_q ($q = 1, 2$) are the inverter-side filter inductor, grid-side filter inductor, and filter capacitor of the qth inverter, respectively; L_g is the grid impedance. In addition, U_{dcq} ($q = 1, 2$) represents the dc-side voltage of the qth inverter; i_{ixq}, i_{gxq}, and i_{cxq} ($x = a, b, c, q = 1, 2$) represent the three-phase inverter-side current, grid-side current and capacitor current of the qth inverter, respectively; u_{px} and i_{sx} ($x = a, b, c$) represent the three-phase point of common coupling (PCC) voltage and the three-phase total grid-connected current, respectively; S_{xq} ($x = a, b, c, q = 1, 2$) represents the three-phase switching signal of the qth inverter; i_g^* is the current reference. Phase disposition pulsewidth modulation (PD-PWM) is adopted, and $\triangle\varphi$ represents the carrier phase difference between two inverters. Both *LCL* GCIs adopt grid-side-current feedback (GCF) PI + capacitor-current-feedback (CCF) active damping (AD) control.

III. HSS Modeling and Harmonic Calculation for Parallel System Considering Asynchronous Carriers

First, based on [12], Section III-A explores the construction method of the complete HSS model for parallel system suitable for frequency-domain analysis and considering asynchronous carriers. Second, based on [13], Section III-B explores the iterative calculation method for the HSS model of parallel system considering asynchronous carriers. Since both [12] and [13] have detailed the HSS modeling principles, this article will not repeat them. In addition, the frequency-domain analysis method and modeling method of the HSS model for the single inverter, as well as the iterative calculation method and modeling method of the HSS model, have been detailed in [12] and [13]. Therefore, this section will study and illustrate the main differences between the modeling analysis of parallel system under asynchronous carriers and the modeling analysis of the single inverter.

A. Complete HSS Model for Parallel System Considering Asynchronous Carriers

To conduct the detailed and accurate analysis of system harmonic characteristics through frequency-domain analysis methods such as pole map, it is necessary to obtain the system harmonic transfer function. Meanwhile, building the complete HSS model of the system is the only means to obtain the harmonic transfer function of the system. Therefore, the construction of the complete HSS model for parallel system is an indispensable step, and it is the prerequisite of the frequency-domain analysis of parallel system. It can be seen from Fig. 2, the model of the parallel system of two *LCL* GCIs consists of three parts, namely the first and second GCI models with closed-loop control and the PCC model. The following will briefly describe the construction process of the above-mentioned three-part models and the complete HSS model of the parallel system.

1) State-Space Model of LCL GCI Considering Closed-Loop Control and Digitization Impact: The state-space modeling process of the single *LCL* GCI based on GCF PI + CCF AD and considering digitization impact has been detailed in [12], and will not be repeated here. Thus, according to [12], the state-space models of two *LCL* GCIs considering digitization impact can be directly obtained.

$$\begin{cases} \text{1st inverter:} \begin{cases} \Delta\dot{\boldsymbol{x}}_{\mathrm{p1}}(t)=\boldsymbol{A}_{\mathrm{p1}}(t)\Delta\boldsymbol{x}_{\mathrm{p1}}(t)+\boldsymbol{B}_{\mathrm{p1}}(t)\Delta\boldsymbol{u}_{\mathrm{p1}}(t) \\ \Delta\boldsymbol{y}_{\mathrm{p1}}(t)=\boldsymbol{C}_{\mathrm{p1}}(t)\Delta\boldsymbol{x}_{\mathrm{p1}}(t) \end{cases} \\ \text{2nd inverter:} \begin{cases} \Delta\dot{\boldsymbol{x}}_{\mathrm{p2}}(t)=\boldsymbol{A}_{\mathrm{p2}}(t)\Delta\boldsymbol{x}_{\mathrm{p2}}(t)+\boldsymbol{B}_{\mathrm{p2}}(t)\Delta\boldsymbol{u}_{\mathrm{p2}}(t) \\ \Delta\boldsymbol{y}_{\mathrm{p2}}(t)=\boldsymbol{C}_{\mathrm{p2}}(t)\Delta\boldsymbol{x}_{\mathrm{p2}}(t) \end{cases} \end{cases} \tag{1}$$

where

$$\Delta\boldsymbol{x}_{\mathrm{p1}}=\begin{bmatrix}\Delta\boldsymbol{x}_{\mathrm{m1}}(t)\\ \Delta\boldsymbol{x}_{\mathrm{c1}}(t)\\ \Delta\boldsymbol{x}_{\mathrm{d1}}(t)\end{bmatrix},$$

$$\Delta\boldsymbol{x}_{\mathrm{m1}}=\begin{bmatrix}\Delta i_{\mathrm{ia1}}(t) & \Delta i_{\mathrm{ib1}}(t) & \Delta i_{\mathrm{ic1}}(t) & \Delta i_{\mathrm{ga1}}(t) & \Delta i_{\mathrm{gb1}}(t)\\ \Delta i_{\mathrm{gc1}}(t) & \Delta u_{\mathrm{ca1}}(t) & \Delta u_{\mathrm{cb1}}(t) & \Delta u_{\mathrm{cc1}}(t) & \Delta u_{\mathrm{dc1}}(t)\end{bmatrix}^{\mathrm{T}},$$

$$\Delta\boldsymbol{x}_{\mathrm{c1}}(t)=\begin{bmatrix}\Delta e_{\mathrm{d1}}(t) & \Delta e_{\mathrm{q1}}(t)\end{bmatrix}^{\mathrm{T}},$$

$$\Delta\boldsymbol{x}_{\mathrm{d1}}(t)=\begin{bmatrix}\Delta x_{\mathrm{idd1}}(t) & \Delta x_{\mathrm{idq1}}(t)\end{bmatrix}^{\mathrm{T}},$$

$$\Delta\boldsymbol{u}_{\mathrm{p1}}(t)=\begin{bmatrix}\Delta i_{\mathrm{ga1}}{}^{*}(t) & \Delta i_{\mathrm{gb1}}{}^{*}(t) & \Delta i_{\mathrm{gc1}}{}^{*}(t)\\ \Delta u_{\mathrm{pa}}(t) & \Delta u_{\mathrm{pb}}(t) & \Delta u_{\mathrm{pc}}(t)\end{bmatrix}^{T},$$

$$\Delta\boldsymbol{y}_{\mathrm{p1}}(t)=\begin{bmatrix}\Delta i_{\mathrm{ga1}}(t) & \Delta i_{\mathrm{gb1}}(t) & \Delta i_{\mathrm{gc1}}(t)\end{bmatrix}^{\mathrm{T}},$$

$$\boldsymbol{A}_{\mathrm{p1}}(t)=\begin{bmatrix}\boldsymbol{A}_{\mathrm{s1}}(t)+\boldsymbol{B}_{\mathrm{s1}}(t)[\boldsymbol{K}_{\mathrm{s1}}(t)+\boldsymbol{L}_{\mathrm{s1}}(t)\boldsymbol{G}_{\mathrm{s1}}(t)]\\ \boldsymbol{I}_{\mathrm{s1}}(t)+\boldsymbol{J}_{\mathrm{s1}}(t)\boldsymbol{G}_{\mathrm{s1}}(t)\\ \boldsymbol{E}_{\mathrm{s1}}(t)\end{bmatrix},$$

$$\boldsymbol{B}_{\mathrm{p1}}(t)=\begin{bmatrix}\boldsymbol{B}_{\mathrm{s1}}(t)\boldsymbol{L}_{\mathrm{s1}}(t)\boldsymbol{H}_{\mathrm{s1}}(t)\\ \boldsymbol{J}_{\mathrm{s1}}(t)\boldsymbol{H}_{\mathrm{s1}}(t)\\ \boldsymbol{F}_{\mathrm{s1}}(t)\end{bmatrix},\ \boldsymbol{C}_{\mathrm{p1}}(t)=\boldsymbol{C}_{\mathrm{s1}}(t).$$

The specific expressions of matrices $\boldsymbol{A}_{\mathrm{s1}}(t)$, $\boldsymbol{B}_{\mathrm{s1}}(t)$, $\boldsymbol{C}_{\mathrm{s1}}(t)$, $\boldsymbol{E}_{\mathrm{s1}}(t)$, $\boldsymbol{F}_{\mathrm{s1}}(t)$, $\boldsymbol{G}_{\mathrm{s1}}(t)$, $\boldsymbol{H}_{\mathrm{s1}}(t)$, $\boldsymbol{I}_{\mathrm{s1}}(t)$, $\boldsymbol{J}_{\mathrm{s1}}(t)$, $\boldsymbol{K}_{\mathrm{s1}}(t)$, $\boldsymbol{L}_{\mathrm{s1}}(t)$ can be referred to (A4)–(A6) in [12]. Specifically, by replacing the corresponding parameter symbols in (A4)–(A6) of [12] with the parameter symbols of the first inverter in Fig. 2, and replacing $L_{2\mathrm{total}}$ with L_{12}, then the specific expressions for $\boldsymbol{A}_{\mathrm{s1}}(t)$, $\boldsymbol{B}_{\mathrm{s1}}(t)$, $\boldsymbol{C}_{\mathrm{s1}}(t)$, $\boldsymbol{E}_{\mathrm{s1}}(t)$, $\boldsymbol{F}_{\mathrm{s1}}(t)$, $\boldsymbol{G}_{\mathrm{s1}}(t)$, $\boldsymbol{H}_{\mathrm{s1}}(t)$, $\boldsymbol{I}_{\mathrm{s1}}(t)$, $\boldsymbol{J}_{\mathrm{s1}}(t)$, $\boldsymbol{K}_{\mathrm{s1}}(t)$, $\boldsymbol{L}_{\mathrm{s1}}(t)$ can be obtained. The expression and acquisition method of the state variable $\triangle\boldsymbol{x}_{\mathrm{p2}}(t)$, input $\triangle\boldsymbol{u}_{\mathrm{p2}}(t)$, output $\triangle\boldsymbol{y}_{\mathrm{p2}}(t)$, and matrices $\boldsymbol{A}_{\mathrm{s2}}(t)$, $\boldsymbol{B}_{\mathrm{s2}}(t)$, $\boldsymbol{C}_{\mathrm{s2}}(t)$, $\boldsymbol{E}_{\mathrm{s2}}(t)$, $\boldsymbol{F}_{\mathrm{s2}}(t)$, $\boldsymbol{G}_{\mathrm{s2}}(t)$, $\boldsymbol{H}_{\mathrm{s2}}(t)$, $\boldsymbol{I}_{\mathrm{s2}}(t)$, $\boldsymbol{J}_{\mathrm{s2}}(t)$, $\boldsymbol{K}_{\mathrm{s2}}(t)$, $\boldsymbol{L}_{\mathrm{s2}}(t)$ in the second inverter are the same as those in the first inverter.

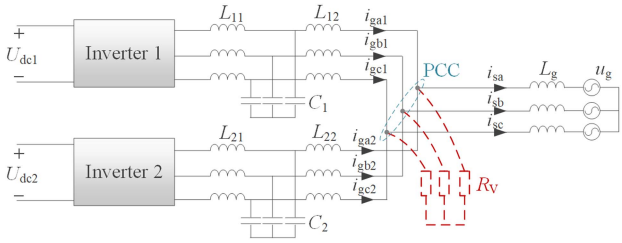

Fig. 3. Introducing a large-resistance virtual load R_{V} at PCC (only for the modeling process).

Then, (1) can be expressed as a state-space equation as follows:

$$\begin{cases}\Delta\dot{\boldsymbol{x}}_{\mathrm{pt}}(t)=\boldsymbol{A}_{\mathrm{pt}}(t)\Delta\boldsymbol{x}_{\mathrm{pt}}(t)+\boldsymbol{B}_{\mathrm{pt}}(t)\Delta\boldsymbol{u}_{\mathrm{pt}}(t)\\ \Delta\boldsymbol{y}_{\mathrm{pt}}(t)=\boldsymbol{C}_{\mathrm{pt}}(t)\Delta\boldsymbol{x}_{\mathrm{pt}}(t)\end{cases} \tag{2}$$

where

$$\Delta\boldsymbol{x}_{\mathrm{pt}}(t)=\begin{bmatrix}\Delta\boldsymbol{x}_{\mathrm{p1}}(t)\\ \Delta\boldsymbol{x}_{\mathrm{p2}}(t)\end{bmatrix},\quad \Delta\boldsymbol{u}_{\mathrm{pt}}(t)=\begin{bmatrix}\Delta\boldsymbol{u}_{\mathrm{p1}}(t)_{(l1\sim l3)}\\ \Delta\boldsymbol{u}_{\mathrm{p2}}(t)_{(l1\sim l3)}\\ \Delta\boldsymbol{u}_{\mathrm{p2}}(t)_{(l4\sim l6)}\end{bmatrix},$$

$$\Delta\boldsymbol{y}_{\mathrm{pt}}(t)=\begin{bmatrix}\Delta\boldsymbol{y}_{\mathrm{p1}}(t)\\ \Delta\boldsymbol{y}_{\mathrm{p2}}(t)\end{bmatrix}.$$

Here, the subscripts ($l1$–$l3$) and ($l4$–$l6$) represent the 1st–3rd rows and the 4th–6th rows of the matrix, respectively. The specific expressions for $\boldsymbol{A}_{\mathrm{pt}}(t)$, $\boldsymbol{B}_{\mathrm{pt}}(t)$, and $\boldsymbol{C}_{\mathrm{pt}}(t)$ are detailed in (A1) in Appendix A of this article.

2) State-Space Model of PCC: Due to the presence of inductive grid impedance behind the PCC, an additional state variable needs to be added to the parallel system, namely the total grid-connected current $i_{\mathrm{s}x}(t)$ ($x=$ a, b, c). Then, the relationship between PCC voltage, voltage drop on grid impedance, and grid voltage can be obtained as follows:

$$\Delta u_{\mathrm{p}x}(t)-L_{\mathrm{g}}\frac{\mathrm{d}\Delta i_{\mathrm{s}x}(t)}{\mathrm{d}t}=\Delta u_{\mathrm{g}x}(t),\quad x=\mathrm{a},\mathrm{b},\mathrm{c}. \tag{3}$$

In the process of converting (3) into the state-space equation, it can be found that $\triangle u_{\mathrm{p}x}(t)$ is neither a state variable nor an input variable. Thus, in order to complete the above-mentioned transformation, corresponding measures need to be taken. Here, it should be noted, the state-space models of PCC and two *LCL* GCIs ultimately need to be integrated into a whole, which is inevitably more complex and of higher order. In order to maximize the computational efficiency of the complete model, the total number of state variables in the parallel system should be minimized. Therefore, during the modeling process, a virtual load R_{V} with large resistance is introduced to PCC, as shown in Fig. 3.

In this way, $\triangle u_{\mathrm{p}x}(t)$ can be characterized by existing state variables, as shown in the following equation:

$$\Delta u_{\mathrm{p}x}(t)=R_{\mathrm{V}}(\Delta i_{\mathrm{g}x1}(t)+\Delta i_{\mathrm{g}x2}(t)-\Delta i_{\mathrm{s}x}(t)),\quad x=\mathrm{a},\mathrm{b},\mathrm{c}. \tag{4}$$

3) Complete State-Space Model of Parallel System: In order to derive the harmonic transfer function of the parallel system, it is necessary to use a complete state-space equation to describe the entire parallel system. Therefore, (2)–(4) need to be reconstructed.

First, reconstruct the state-space (2) of the two GCIs considering digitization impact. We can obtain

$$\begin{cases}\Delta\dot{\boldsymbol{x}}_{\rm pt}(t)=\boldsymbol{A}_{\rm cp}(t)\Delta\boldsymbol{x}_{\rm cp}(t)+\boldsymbol{B}_{\rm pt}(t)\Delta\boldsymbol{u}_{\rm pt}(t)\\ \Delta\boldsymbol{y}_{\rm pt}(t)=\boldsymbol{C}_{\rm cp}(t)\Delta\boldsymbol{x}_{\rm cp}(t)\end{cases}\tag{5}$$

where the specific expressions of $\boldsymbol{A}_{\rm cp}(t)$ and $\boldsymbol{C}_{\rm cp}(t)$ are detailed in (A2) of Appendix A, and

$$\Delta\boldsymbol{x}_{\rm cp}(t)=\begin{bmatrix}\Delta\boldsymbol{x}_{\rm pt}(t)\\ \Delta i_{\rm sa}(t)\\ \Delta i_{\rm sb}(t)\\ \Delta i_{\rm sc}(t)\end{bmatrix}.$$

Second, reconstruct the state-space model (3) of PCC

$$\Delta\boldsymbol{u}_{\rm pt}(t)=\boldsymbol{M}_{\rm cp}(t)\Delta\boldsymbol{x}_{\rm cp}(t)+\boldsymbol{N}_{\rm cp}(t)\Delta\boldsymbol{u}_{\rm cp}(t)\tag{6}$$

where the specific expressions of $\boldsymbol{M}_{\rm cp}(t)$ and $\boldsymbol{N}_{\rm cp}(t)$ are detailed in (A3) of Appendix A, and

$$\Delta\boldsymbol{u}_{\rm cp}(t)=\begin{bmatrix}\Delta\boldsymbol{u}_{\rm pt}(t)_{(l1\sim l6)}\\ \Delta u_{\rm ga}(t)\\ \Delta u_{\rm gb}(t)\\ \Delta u_{\rm gc}(t)\end{bmatrix}.$$

Finally, reconstruct the state-space model (4) of PCC

$$\Delta\dot{\boldsymbol{x}}_{\rm gp}(t)=\boldsymbol{O}_{cp}(t)\Delta\boldsymbol{x}_{\rm cp}(t)+\boldsymbol{P}_{\rm cp}(t)\Delta\boldsymbol{u}_{\rm cp}(t)\tag{7}$$

where the specific expressions of $\boldsymbol{O}_{\rm cp}(t)$ and $\boldsymbol{P}_{\rm cp}(t)$ are detailed in (A4) of Appendix A, and

$$\Delta\boldsymbol{x}_{\rm gp}(t)=\begin{bmatrix}\Delta i_{\rm sa}(t) & \Delta i_{\rm sb}(t) & \Delta i_{\rm sc}(t)\end{bmatrix}^{\rm T}.$$

Substituting (6) into (5) and combining (7), the complete state-space model of the inverter parallel system considering digitization impact can be obtained as follows:

$$\begin{cases}\Delta\dot{\boldsymbol{x}}_{\rm par}(t)=\boldsymbol{Q}_{\rm cp}(t)\Delta\boldsymbol{x}_{\rm par}(t)+\boldsymbol{R}_{\rm cp}(t)\Delta\boldsymbol{u}_{\rm par}(t)\\ \Delta\boldsymbol{y}_{\rm par}(t)=\boldsymbol{S}_{\rm cp}(t)\Delta\boldsymbol{x}_{\rm par}(t)\end{cases}\tag{8}$$

where

$$\Delta\boldsymbol{x}_{\rm par}(t)=\begin{bmatrix}\Delta\boldsymbol{x}_{\rm cp}(t)\\ \Delta\boldsymbol{x}_{\rm gp}(t)\end{bmatrix},\Delta\boldsymbol{u}_{\rm par}(t)=\Delta\boldsymbol{u}_{\rm cp}(t),$$

$$\Delta\boldsymbol{y}_{\rm par}(t)=\begin{bmatrix}\Delta\boldsymbol{y}_{\rm pt}(t)\\ \Delta\boldsymbol{x}_{\rm gp}(t)\end{bmatrix},$$

$$\boldsymbol{Q}_{\rm cp}(t)=\begin{bmatrix}\boldsymbol{A}_{\rm cp}(t)+\boldsymbol{B}_{\rm pt}(t)\boldsymbol{M}_{\rm cp}(t)\\ \boldsymbol{O}_{\rm cp}(t)\end{bmatrix},$$

$$\boldsymbol{R}_{\rm cp}(t)=\begin{bmatrix}\boldsymbol{B}_{\rm pt}(t)\boldsymbol{N}_{\rm cp}(t)\\ \boldsymbol{P}_{\rm cp}(t)\end{bmatrix},$$

$$\boldsymbol{S}_{\rm cp}(t)=\begin{bmatrix}\boldsymbol{C}_{\rm cp}(t)\\ \cdots\cdots\cdots\cdots\\ \boldsymbol{Z}_{3\times28}\ \vdots\ \boldsymbol{I}_3\end{bmatrix}.$$

4) Complete HSS Model of Parallel System Considering Asynchronous Carriers: Combining the HSS modeling steps [12], [13] and the complete state-space model (8) of parallel system considering digitization impact, the complete HSS model of parallel system considering digitization impact can finally be obtained.

$$\begin{cases}\dot{\boldsymbol{X}}_{\rm parh}=(\mathcal{Q}_{\rm parh}-\boldsymbol{N}_{\rm parh})\boldsymbol{X}_{\rm parh}+\mathcal{R}_{\rm parh}\boldsymbol{U}_{\rm parh}\\ \boldsymbol{Y}_{\rm parh}=\boldsymbol{S}_{\rm parh}\boldsymbol{X}_{\rm parh}\end{cases}.\tag{9}$$

The state variables, inputs, and outputs in (9) are all in the form of harmonic components of the state variables, inputs, and outputs in (8), and these harmonic components are all expressed in frequency domain. Assuming the truncation number is r, the form of the output $\boldsymbol{Y}_{\rm parh}$ is

$$\boldsymbol{Y}_{\rm parh}=\mathbb{F}\left[\Delta\boldsymbol{i}_{\rm ga1\_-r\sim r}\quad\Delta\boldsymbol{i}_{\rm gb1\_-r\sim r}\quad\Delta\boldsymbol{i}_{\rm gc1\_-r\sim r}\right.$$
$$\Delta\boldsymbol{i}_{\rm ga2\_-r\sim r}\quad\Delta\boldsymbol{i}_{\rm gb2\_-r\sim r}\quad\Delta\boldsymbol{i}_{\rm gc2\_-r\sim r}\quad\Delta\boldsymbol{i}_{\rm sa\_-r\sim r}\quad\Delta\boldsymbol{i}_{\rm sb\_-r\sim r}$$
$$\left.\Delta\boldsymbol{i}_{\rm sc\_-r\sim r}\right]^{\rm T},$$

where taking $\triangle i_{\rm ga1\_-r-r}$ as an example, its form is as follows:

$$\mathbb{F}(\Delta\boldsymbol{i}_{\rm ga1\_-r\sim r})$$
$$=\mathbb{F}\left[\Delta i_{\rm ga1\_-r}\quad\Delta i_{\rm ga1\_-(r-1)}\quad\cdots\quad\Delta i_{\rm ga1\_0}\cdots\right.$$
$$\left.\Delta i_{\rm ga1\_(r-1)}\quad\Delta i_{\rm ga1\_r}\right]^{\rm T}.$$

Here, $\mathbb{F}$ means to convert the time-domain expression of the sinusoidal signal into the frequency-domain expression, and its conversion method can refer to (12) and (13) in [12]. The forms of other state variables, inputs and outputs are similar to the abovementioned. The form of the frequency modulation matrix $\boldsymbol{N}_{\rm parh}$ is similar to (11) in [12], and the dimension is consistent with the matrix $\mathcal{Q}_{\rm parh}$. Since the matrices $\boldsymbol{Q}_{\rm parh}$ and $\boldsymbol{R}_{\rm parh}$ in (8) contain switching functions and Park transformations, after converting them into the HSS model (9), the corresponding matrices will contain periodic variables such as switching functions and trigonometric functions. According to the HSS modeling principle in [12], these matrices [namely $\boldsymbol{Q}_{\rm parh}$ and $\boldsymbol{R}_{\rm parh}$ in (8)] need to be expressed in the form of Toeplitz matrices. Their specific forms can refer to the (10) in [12], and will not be repeated here. While, the matrix $\boldsymbol{S}_{\rm parh}$ does not contain periodic variables, so the form of $\boldsymbol{S}_{\rm parh}$ is similar to the matrix form of (22) in [12].

Finally, the harmonic transfer function of the parallel system with two GCIs can be obtained from (9), namely

$$\boldsymbol{G}_{\rm parh\_HTF}=\boldsymbol{S}_{\rm parh}[s\boldsymbol{I}-(\mathcal{Q}_{\rm parh}-\boldsymbol{N}_{\rm parh})]^{-1}\mathcal{R}_{\rm parh}.\tag{10}$$

In the following, it will be briefly explained how the complete HSS model of the inverter parallel system reflects the carrier phase difference. Based on Appendix A of [12] and Appendix A of this article, it can be seen, the matrix $\boldsymbol{Q}_{\rm parh}$ in (9) contains the amplitude and phase information of the switching function at each harmonic frequency. At the same time, it can be known from the double Fourier series decomposition theory, the carrier phase will affect the spectrum analysis results of the switching function. Thus, the carrier asynchrony is ultimately reflected by the matrix $\mathcal{Q}_{\rm parh}$ in the complete HSS model (9) of parallel

system. Specifically, carrier asynchrony is reflected by the difference in the amplitude and phase of the switching functions of the two inverters in matrix $\mathcal{Q}_{\mathrm{parh}}$.

So far, the complete HSS model of parallel system considering asynchronous carriers has been constructed, and the frequency-domain analysis based on this model will be described in detail in Section IV.

B. Iterative Calculation Method of Parallel-System HSS Model Considering Asynchronous Carriers

As mentioned in Section IV-B of [12] and Section III-C-3 of [13], the iterative calculation process of the HSS model does not need to obtain the complete HSS model of the system. Instead, the state-space models of each part in the GCI system need to be constructed independently and transformed into corresponding HSS models. Then, by assigning corresponding initial values to each state variable and input, and solving the HSS models of each part in the sequence of signal flow, the iterative calculation of the HSS model of grid-connected system can be completed. In the iterative calculation method of HSS models, since the HSS models of each part in the inverter system are independently constructed, these HSS models have fewer state variables and lower orders. Meanwhile, the iterative calculation process of the HSS model does not involve the operation of symbolic expressions, it only needs to solve the differential equation repeatedly, so its calculation efficiency is relatively high. The iterative calculation method of the HSS model can be used to replace circuit simulation and accurately calculate harmonic components of state variables of inverter, and can more intuitively reflect the dynamic characteristic of the system.

Cai et al. [13] have already studied the iterative calculation method of the single-inverter HSS model considering digitization impact and switching frequency. Therefore, this subsection will focus on the additional aspects that need to be considered in the iterative process of the parallel-system HSS model.

1) Independent Construction of HSS Models for the Main Circuit and Control System of Two LCL *GCIs:* In the parallel operation system of two *LCL* GCIs, the HSS models for the main circuit and control system of each inverter are consistent with those in single inverter (namely (19) and (20) in [13]). Therefore, according to (19) in [13], the main-circuit HSS models of two *LCL* GCIs can be directly obtained.

$$\text{1st inverter:}\begin{cases}\dot{\boldsymbol{X}}_{\mathrm{imh1}}=(\mathcal{A}_{\mathrm{ih1}}-\boldsymbol{N}_{\mathrm{m1}})\boldsymbol{X}_{\mathrm{imh1}}+\mathcal{B}_{\mathrm{ih1}}\boldsymbol{U}_{\mathrm{imhr1}}\\ \boldsymbol{Y}_{\mathrm{imh1}}=\boldsymbol{C}_{\mathrm{ih1}}\boldsymbol{X}_{\mathrm{imh1}}\end{cases} \tag{11}$$

$$\text{2nd inverter:}\begin{cases}\dot{\boldsymbol{X}}_{\mathrm{imh2}}=(\mathcal{A}_{\mathrm{ih2}}-\boldsymbol{N}_{\mathrm{m2}})\boldsymbol{X}_{\mathrm{imh2}}+\mathcal{B}_{\mathrm{ih2}}\boldsymbol{U}_{\mathrm{imhr2}}\\ \boldsymbol{Y}_{\mathrm{imh2}}=\boldsymbol{C}_{\mathrm{ih2}}\boldsymbol{X}_{\mathrm{imh2}}\end{cases}. \tag{12}$$

Meanwhile, according to (20) in [13], the control-system HSS models of two *LCL* GCIs can be directly obtained.

$$\text{1st inverter:}\begin{cases}\dot{\boldsymbol{X}}_{\mathrm{ich1}}=(\boldsymbol{E}_{\mathrm{ih1}}-\boldsymbol{N}_{\mathrm{c1}})\boldsymbol{X}_{\mathrm{ich1}}+\mathcal{F}_{\mathrm{ih1}}\boldsymbol{U}_{\mathrm{ich1}}\\ \boldsymbol{Y}_{\mathrm{ich1}}=\mathcal{G}_{\mathrm{ih1}}\boldsymbol{X}_{\mathrm{ich1}}+\mathcal{H}_{\mathrm{ih1}}\boldsymbol{U}_{\mathrm{ich1}}\end{cases} \tag{13}$$

$$\text{2nd inverter:}\begin{cases}\dot{\boldsymbol{X}}_{\mathrm{ich2}}=(\boldsymbol{E}_{\mathrm{ih2}}-\boldsymbol{N}_{\mathrm{c2}})\boldsymbol{X}_{\mathrm{ich2}}+\mathcal{F}_{\mathrm{ih2}}\boldsymbol{U}_{\mathrm{ich2}}\\ \boldsymbol{Y}_{\mathrm{ich2}}=\mathcal{G}_{\mathrm{ih2}}\boldsymbol{X}_{\mathrm{ich2}}+\mathcal{H}_{\mathrm{ih2}}\boldsymbol{U}_{\mathrm{ich2}}\end{cases}. \tag{14}$$

The state variables, inputs, and outputs in (11)–(14) are all in the form of harmonic components. Meanwhile, the specific expressions of state variables, inputs, outputs, and matrices can refer to the relevant content of Section III-C in [13].

However, there is a difference between the HSS models (11) and (12) of the two inverter main circuits in this article and the HSS model (19) of the single inverter main circuit in [13]. In [13], the input $\boldsymbol{U}_{\mathrm{imh}}$ in the HSS model of the main circuit of the single inverter is composed of the grid voltage $u_{\mathrm{g}x}$ and the control system output s_x under frequency domain; while, in this article, the inputs $\boldsymbol{U}_{\mathrm{imhr1}}$ and $\boldsymbol{U}_{\mathrm{imhr2}}$ in HSS models of the main circuit of the two GCIs are composed of the PCC voltage $u_{\mathrm{p}x}$ and the actual switching function $s_x{}'$ after PWM under frequency domain.

2) Construction of PCC Harmonic Model: In the iterative calculation process of the parallel-system HSS model, there is no need to integrate the mathematical models of each part in the parallel system into a whole, so there is no need to unify the state variables of each part, and thus there is no need to introduce the virtual load at PCC. Here, it is enough to write the circuit equation according to the relationship between the PCC voltage and the total grid-connected current, as shown in (3). Then, the harmonic form of (3) can be obtained as shown in the following equation:

$$\boldsymbol{U}_{\mathrm{pcch}}=L_g\frac{\mathrm{d}(\boldsymbol{I}_{\mathrm{g1h}}-\boldsymbol{I}_{\mathrm{g2h}})}{\mathrm{d}t}+\boldsymbol{U}_{\mathrm{gh}} \tag{15}$$

where

$$\boldsymbol{U}_{\mathrm{pcch}}=\mathbb{F}\left[\triangle\,\boldsymbol{u}_{\mathrm{pa\_}-r\sim r}\quad\triangle\,\boldsymbol{u}_{\mathrm{pb\_}-r\sim r}\quad\triangle\,\boldsymbol{u}_{\mathrm{pc\_}-r\sim r}\right],$$

$$\boldsymbol{I}_{\mathrm{g1h}}=\mathbb{F}\left[\triangle\,\boldsymbol{i}_{\mathrm{ga1\_}-r\sim r}\quad\triangle\,\boldsymbol{i}_{\mathrm{gb1\_}-r\sim r}\quad\triangle\,\boldsymbol{i}_{\mathrm{gc1\_}-r\sim r}\right],$$

$$\boldsymbol{I}_{\mathrm{g2h}}=\mathbb{F}\left[\triangle\,\boldsymbol{i}_{\mathrm{ga2\_}-r\sim r}\quad\triangle\,\boldsymbol{i}_{\mathrm{gb2\_}-r\sim r}\quad\triangle\,\boldsymbol{i}_{\mathrm{gc2\_}-r\sim r}\right].$$

$$\mathbf{U}_{\mathrm{gh}}=\mathbb{F}\left[\triangle\,\boldsymbol{u}_{\mathrm{ga\_}-r\sim r}\quad\triangle\,\boldsymbol{u}_{\mathrm{gb\_}-r\sim r}\quad\triangle\,\boldsymbol{u}_{\mathrm{gc\_}-r\sim r}\right].$$

3) Iterative Calculation Process of Parallel-System HSS Model Considering Asynchronous Carriers, Switching Frequency, and Digitization Impact: The iterative calculation process of the parallel-system HSS model considering asynchronous carriers, switching frequency, and digitization impact is shown in Fig. 4. Wherein, the methods of considering the switching frequency and digitization impact have been detailed in Section III-C-3 of [13], so it will not be repeated here. The following will focus on explaining the difference between the iterative calculation process of the parallel-system HSS model shown in Fig. 4 and that of the single-inverter HSS model shown in Fig. 4 of [13].

1) The iterative calculation of the parallel-system HSS model shown in Fig. 4 considers the PD-PWM process, namely *Step* s5. In this way, the carrier phase difference between the two inverters can be directly set. It should be noted, the PWM process is completed in time domain, while the other processes in Fig. 4 are completed in frequency domain. Therefore, before s5 and after s5, the

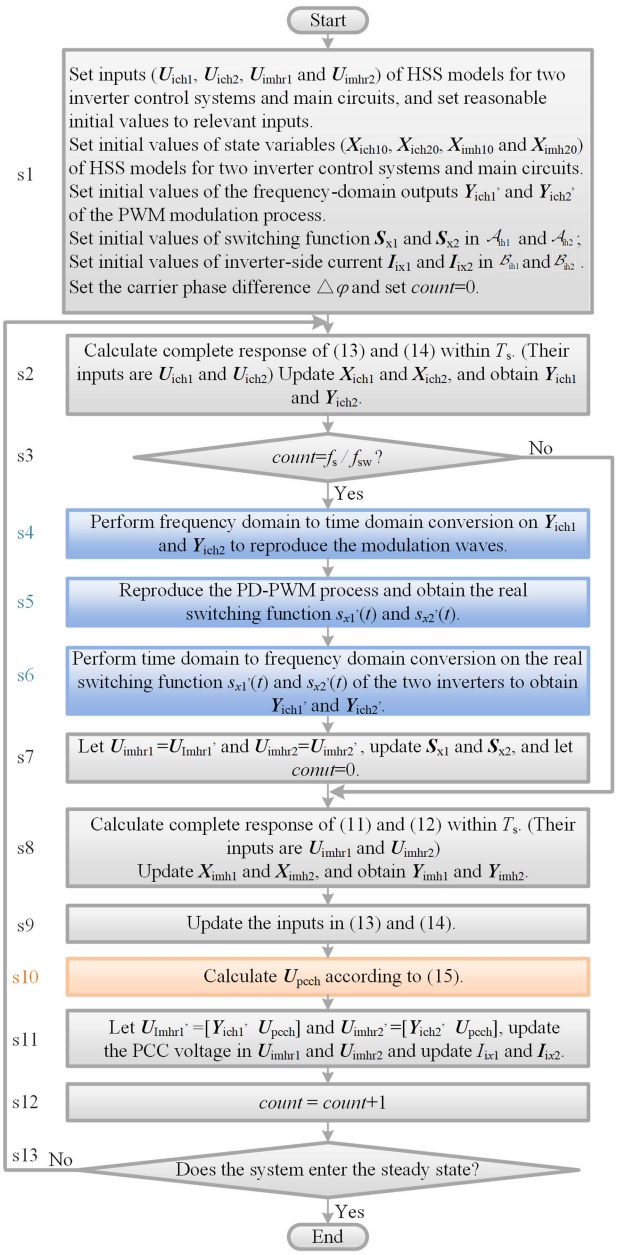

Fig. 4. Iterative calculation process of HSS model for inverter parallel system considering asynchronous carriers.

conversion of frequency domain to time domain and time domain to frequency domain needs to be performed, respectively. The above-mentioned steps are reflected in blue shaded area in Fig. 4. Among them, $s_{x1}'(t)$ and $s_{x2}'(t)$ represent the actual switching function obtained after PWM; Y_{ich1}' and Y_{ich2}' are frequency-domain representations of $s_{x1}'(t)$ and $s_{x2}'(t)$, respectively.

2) The iterative calculation process of the parallel-system HSS model adds the calculation and update of PCC voltage. This step is reflected in orange shaded area in Fig. 4.

TABLE I
PARALLEL SYSTEM PARAMETERS OF HIGH-POWER *LCL* GCIS (SYSTEM PARAMETER I)

Parameter	Value	Parameter	Value
Power (P_1, P_2)	100 kW	DC-side voltage (U_{dc})	700 V
Switching frequency (f_{sw})	2 kHz	RMS value of grid line-to-line voltage (u_{gx_l})	315 V
Sampling frequency (f_s)	10 kHz	Grid impedance (L_g)	0.6 mH
Filter inductors (L_{11}, L_{21})	0.52 mH	Controller proportional gain (k_{p1}, k_{p2})	1
Filter inductors (L_{12}, L_{22})	0.26 mH	Controller integral gain (k_{i1}, k_{i2})	1000
Filter capacitors (C_1, C_2)	158 μF	Active damping coefficient (k_{c1}, k_{c2})	1

TABLE II
PARALLEL SYSTEM PARAMETERS OF LOW-POWER *LCL* GCIS (SYSTEM PARAMETER II)

Parameter	Value	Parameter	Value
Power (P_1, P_2)	250 W	DC-side voltage (U_{dc})	100 V
Switching frequency (f_{sw})	2 kHz	RMS value of grid line-to-line voltage (u_{gx_l})	18 V
Sampling frequency (f_s)	10 kHz	Grid impedance (L_g)	1.75 mH
Filter inductors (L_{11}, L_{21})	4 mH	Controller proportional gain (k_{p1}, k_{p2})	1.4
Filter inductors (L_{12}, L_{22})	2 mH	Controller integral gain (k_{i1}, k_{i2})	1000
Filter capacitors (C_1, C_2)	15 μF	Active damping coefficient (k_{c1}, k_{c2})	1.4

The accuracy verification of the proposed iterative-calculation process will be described in detail in Section V.

IV. FREQUENCY-DOMAIN ANALYSIS AND VALIDATION OF THE COMPLETE HSS MODEL FOR PARALLEL SYSTEM

This section will analyze frequency-domain characteristics of the system in detail based on the complete HSS model of parallel system derived in Section III-A. The impact of asynchronous carriers on system characteristics is explained, and the effectiveness and accuracy of the complete HSS model for parallel system are verified. The parameters of the parallel system of LSF high-power *LCL* GCIs are shown in Table I.

At the same time, in order to intuitively compare the frequency-domain analysis results and simulation results with the subsequent experimental data, this section also sets a set of low-power parallel system parameters according to the experimental platform, as shown in Table II. Therefore, the system characteristic analysis and related verification involved in this section will be completed under two sets of system parameters. Under different system parameters, this section will conduct a detailed analysis of the characteristics of parallel system considering asynchronous carriers through the harmonic coupling diagrams and gain diagrams of grid voltage to output current, and pole maps of current reference to output current. In addition, the truncation number of the HSS model in this article is selected as 40; the asynchronous carrier takes the carrier phase difference of 120° as an example.

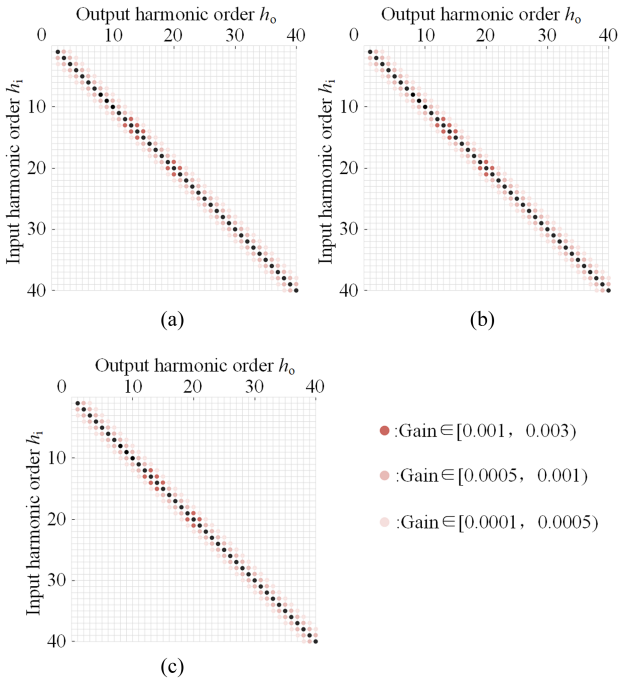

Fig. 5. Schematic diagrams of harmonic coupling between grid voltage and output current under synchronous carriers. (a) i_{ga1_ho}/u_{ga_hi}. (b) i_{ga2_ho}/u_{ga_hi}. (c) i_{sa_ho}/u_{ga_hi}.

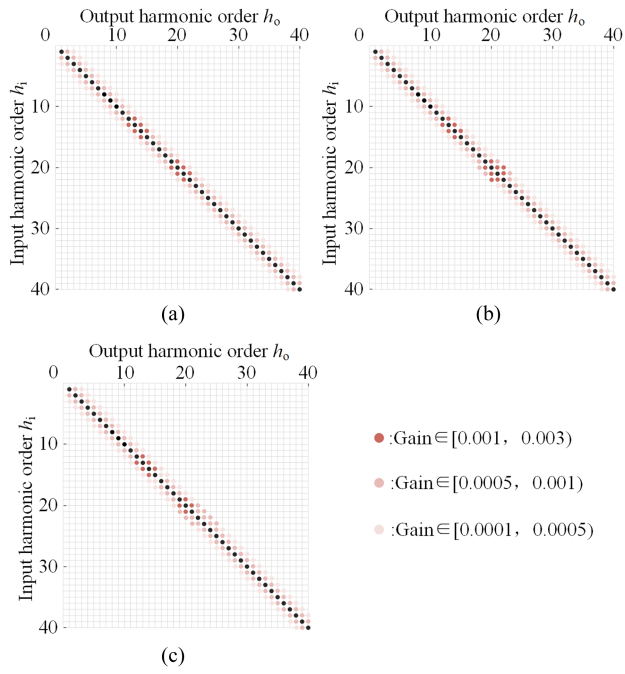

Fig. 6. Schematic diagrams of harmonic coupling between grid voltage and output current when the carrier phase difference is 120°. (a) i_{ga1_ho}/u_{ga_hi}. (b) i_{ga2_ho}/u_{ga_hi}. (c) i_{sa_ho}/u_{ga_hi}.

A. Frequency-Domain Analysis and Verification Under Parallel System Parameter I

1) Characteristic Analysis of Grid Voltage to Output Current:

a) Coupling analysis of grid voltage to output current: First, when the carriers of two GCIs are completely synchronized, taking phase a as an example, the harmonic coupling diagrams of i_{ga1_ho}/u_{ga_hi}, i_{ga2_ho}/u_{ga_hi} and i_{sa_ho}/u_{ga_hi} are shown in Fig. 5, where h_o∈[0, 40], h_i∈[0, 40]. It can be seen that their off-diagonal terms all have nonzero gains under synchronous carriers. However, further observation shows that the gains of these off-diagonal terms (i.e., coupling gains) are all less than 0.001, which can be ignored. The situation is similar for phases b and c. Therefore, when the carriers are synchronized, the harmonics in the grid basically only affect the output current components of inverter with the same frequency. Furthermore, by carefully observing Fig. 5, the harmonic coupling diagrams corresponding to i_{ga1_ho}/u_{ga_hi}, i_{ga2_ho}/u_{ga_hi}, and i_{sa_ho}/u_{ga_hi} under synchronous carriers are completely consistent. This indicates that the antidisturbance characteristics of the output current of each inverter to the grid voltage are completely consistent under synchronous carriers.

Second, when the carriers of two GCIs differ by 120°, taking phase a as an example, the harmonic coupling diagrams of i_{ga1_ho}/u_{ga_hi}, i_{ga2_ho}/u_{ga_hi}, and i_{sa_ho}/u_{ga_hi} are shown in Fig. 6. It is obvious that when the carriers are not synchronized, there is harmonic coupling phenomenon between the grid voltage and output current. Meanwhile, there are differences in harmonic characteristic between i_{ga1_ho}/u_{ga_hi}, i_{ga2_ho}/u_{ga_hi}, and i_{sa_ho}/u_{ga_hi}. However, careful observation shows that the harmonic coupling between the grid voltage and output current can also be ignored. Therefore, it can be considered that when the carriers are not synchronized, the grid harmonics also only affect the output current components of inverter with the same frequency.

b) Gain analysis of uncoupled terms for grid voltage to output current: From the above-mentioned analysis, regardless of whether the carriers are synchronous or not, the grid harmonics only affect the inverter output current components with the same frequency. Therefore, the following will focus on the detailed analysis of the uncoupled terms (i.e., i_{ga1_h}/u_{ga_h}, i_{ga2_h}/u_{ga_h}, and i_{sa_h}/u_{ga_h}) between the grid voltage and the output current.

First, the gain diagrams of uncoupled terms between the grid voltage and the output current under synchronous carriers are shown in Fig. 7(a). i_{ga1_h}/u_{ga_h} of the first inverter is exactly the same as the i_{ga2_h}/u_{ga_h} of the second inverter. This is reasonable, because the system parameters of the two inverters are completely consistent, so when the carriers are synchronized, all characteristics of the two inverters should theoretically be identical. In addition, as shown in Fig. 7(a), the gain of i_{sa_h}/u_{ga_h} is always twice that of i_{ga1_h}/u_{ga_h} and i_{ga2_h}/u_{ga_h}.

Second, when the carrier phase difference between the two inverters is 120°, the gain diagrams of uncoupled terms between the grid voltage and output current are shown in Fig. 7(b). Comparing Fig. 7(b) with Fig. 7(a), it can be found, the low-frequency gain (≤10th) of the uncoupled terms between the grid voltage and the output current is basically the same; there is a slight

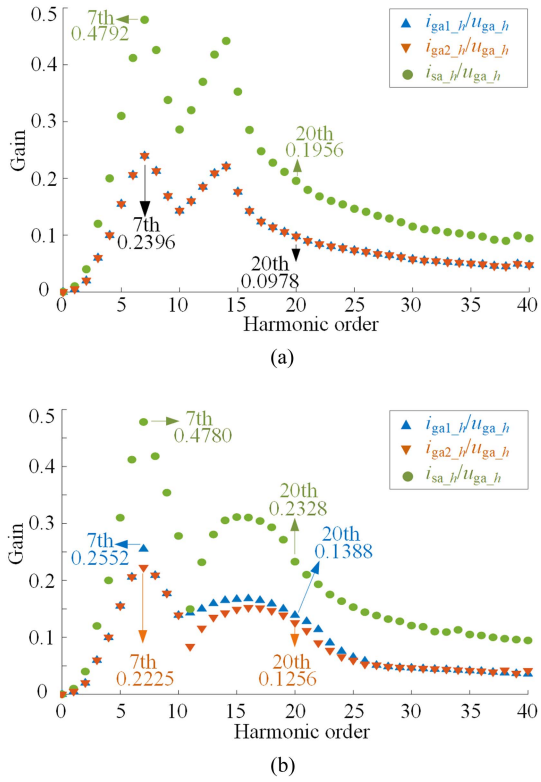

Fig. 7. Gain diagrams of uncoupled terms between grid voltage and output current. (a) Carrier synchronization. (b) Carrier phase difference of 120°.

difference in high-frequency gain (≥27th), and there is a significant difference in mid-frequency gain (11th–26th). In addition, comparing i_{ga1_h}/u_{ga_h} and i_{ga2_h}/u_{ga_h} in Fig. 7(b), it can be seen, there are also some slight differences in mid-frequency characteristics (11th–26th) between the grid voltage and the output current of each inverter. Next, the reasons why asynchronous carriers have the impact on the mid-frequency characteristics between grid voltage and output current will be briefly analyzed. First of all, asynchronous carrier phase will lead to inconsistency of the instantaneous switching sequence of the power switching devices in each inverter, so the two inverters will generate energy interaction through the PCC. Due to the existence of the control system and the *LCL* filter, the low-frequency and high-frequency equivalent output impedances of each inverter are relatively large; in contrast, due to the existence of the resonant peak of the *LCL* filter, the mid-frequency output impedance of each inverter is relatively small, so the energy interaction between the two inverters is mainly dominated by mid-frequency harmonics. Meanwhile, the LSF *LCL* GCI itself has mid-frequency harmonic coupling when the inverter operates alone. Therefore, the mid-frequency resonance generated by asynchronous carriers interacts with the inherent mid-frequency harmonic coupling of the inverter, changing the original mid-frequency characteristics of each inverter. In addition, a brief explanation is provided on the mechanism of the difference in mid-frequency characteristics between the two inverters under asynchronous carriers. According to the theory of double Fourier series decomposition, when the carrier phase of two inverters is inconsistent, the phase of sideband harmonics generated by modulation in the two inverters will also be different, but the change in carrier phase will not affect the amplitude of the sideband harmonics. However, due to the existence of mid-frequency harmonic coupling in LSF *LCL* GCI, the phase of the output-voltage sideband harmonics of the inverter located in mid-frequency region will indirectly affect the amplitude of the mid-frequency harmonics of the output current, thereby affecting the mid-frequency harmonic coupling characteristics of the output current. Thus, the carrier phase will affect the mid-frequency harmonic coupling characteristics of LSF *LCL* GCI. In other words, when the carriers are not synchronized, there will be slight differences in mid-frequency harmonic coupling characteristics of the two inverters themselves, that is, there will be differences in the mid-frequency characteristics of the two inverters.

The accuracy of the proposed model needs to be further verified by comparison with the circuit simulation results, which will be illustrated in Section IV-A-3).

2) Characteristic Analysis of Current Reference to Output Current: When the carriers are synchronized, the pole maps between the current reference and the output current of the two inverters are shown in Fig. 8. Among them, the central poles are marked in black, which are the poles corresponding to the transfer function between the current reference and its output current component at the same frequency, that is, the poles obtained based on SSAV model. The remaining poles are symmetrical about the central poles, and they are the corresponding poles of the transfer function between the current reference and other harmonic components of the output current. It is obvious that all poles are on the left side of the complex plane, indicating that the system is stable. Wherein, the 11th and 12th groups of poles are the dominant poles of the system, and these two groups of poles are conjugate. So, here, we will only use the 0–40th poles in the 11th group of poles as an example to locally enlarge them. In locally enlarged figure, the pole maps of $i_{ga1\_h}/i_{ga1}{}^*$ and $i_{ga2\_h}/i_{ga2}{}^*$ completely overlap. This is because under the premise that the system parameters and carrier phase of the two inverters are identical, the characteristics of the two inverters are theoretically identical.

When the carrier phase difference between two inverters is 120°, the pole maps between the current reference and the output current of the two inverters are shown in Fig. 9. Through data comparison, it can be found, the positions of all central poles in Figs. 8 and 9 are completely consistent, but there are differences in the positions of all poles except for the central poles. Similarly, enlarge the dominant poles (0–40th poles in the 11th group) that can reflect the characteristic of the system. Through careful observation, the mid-frequency pole position near the 20th, namely the part marked by a black circle, is significantly different from that under synchronous carriers; while the low-frequency and high-frequency pole positions are similar to that under synchronous carriers. The above-mentioned phenomenon shows that compared with the condition when the carriers are synchronous, the asynchronous carrier condition causes the change in mid-frequency harmonic stability of each inverter in parallel system. Specifically, under the system parameters shown in Table I, when the carrier of the second inverter

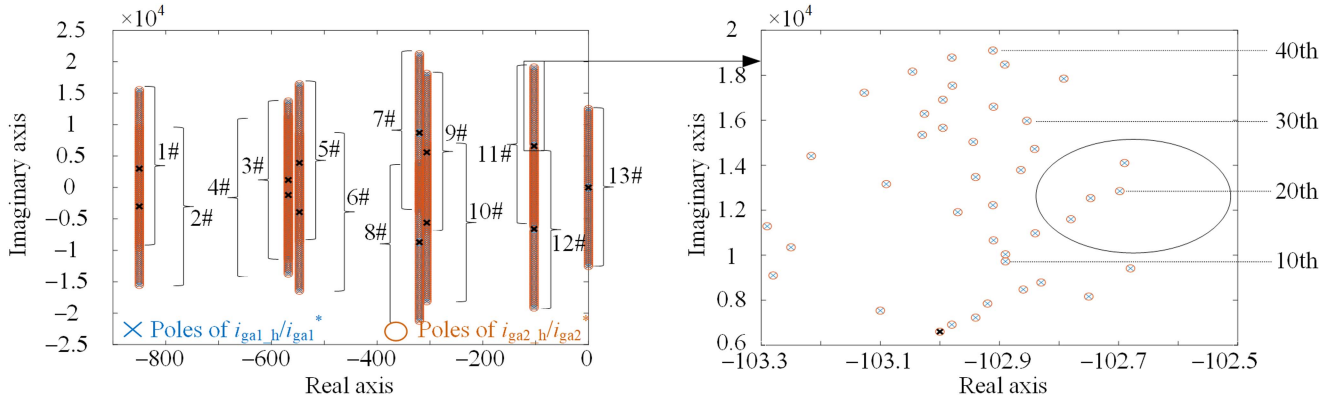

Fig. 8. Pole maps of i_{ga1_h}/i_{ga1}^* and i_{ga2_h}/i_{ga2}^* under synchronous carriers.

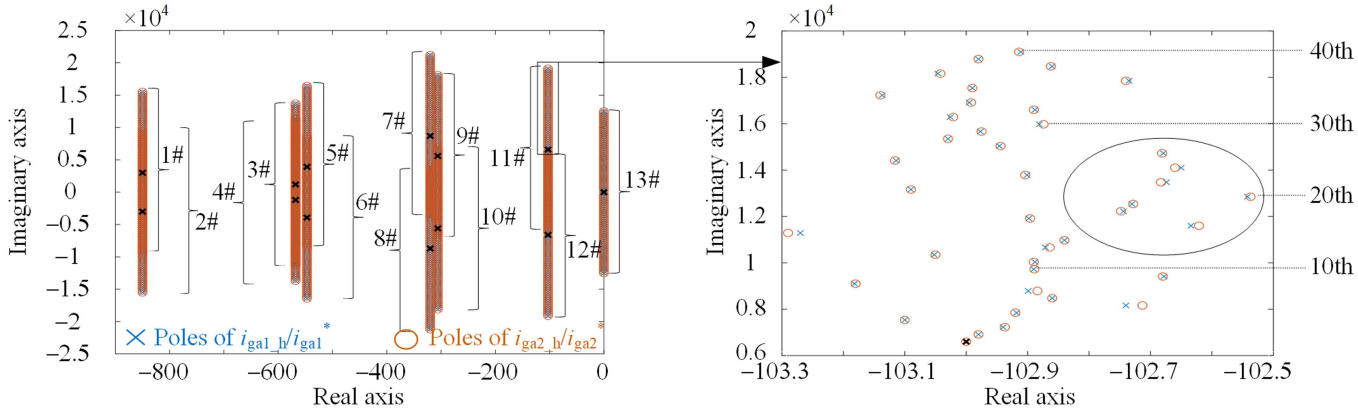

Fig. 9. Pole maps of i_{ga1_h}/i_{ga1}^* and i_{ga2_h}/i_{ga2}^* under asynchronous carriers.

lags by 120°, the stability of the mid-frequency harmonics near the 20th in each inverter deteriorates slightly. The mechanism of the above-mentioned phenomenon is similar to that of Section IV-A-1–b.

In summary, first, the asynchronous carriers will affect the mid-frequency harmonic stability of each inverter in parallel system. Second, the complete HSS model of parallel system proposed, in this article, can reflect the impact of asynchronous carriers on the harmonic stability of the output current of each inverter. Therefore, this model can also be used to analyze the harmonic instability of critically stable or divergent system in the case of asynchronous carriers in detail and accurately.

3) Circuit Simulation Verification: Based on the parallel system structure of *LCL* GCIs shown in Fig. 2, Simulink circuit simulation analysis is carried out under the system parameters shown in Table I, to further verify the accuracy of the complete HSS model of the parallel system proposed in Section III-A.

In the case of carrier synchronization between two inverters, when the grid voltage is ideal, with 5% 7th harmonic and 5% 20th harmonic, the output waveforms of the two inverters and the total grid-connected current are shown in Fig. 10, and the corresponding FFT analysis is shown in Fig. 11. When the carriers are synchronized, no matter what the grid environment is, the FFT analysis results of the output current of the two GCIs and the total grid-connected current are always consistent. The above-mentioned circuit simulation results show that the harmonic characteristics of the two inverters are completely consistent when the carriers are synchronized, which indirectly illustrates the correctness of the analysis results in Sections IV-A-1 and IV-A-2. In addition, by analyzing the data in Fig. 11, when there is 5% 7th harmonic in the grid voltage ($u_{ga\_7\_peak}$ = 12.85 V), the 7th harmonic in the output current of each inverter will be significantly affected. The distortion rate of 7th current harmonic of each inverter increases by 1.237%, so the amplitudes of $\triangle i_{ga1\_7}/\triangle u_{ga\_7}$ and $\triangle i_{ga2\_7}/\triangle u_{ga\_7}$ are both 0.2479, and the amplitude of $\triangle i_{sa\_7}/\triangle u_{ga\_7}$ is 0.4958. Similarly, when there is 5% 20th harmonic in the grid voltage ($u_{ga\_20\_peak}$ = 12.85 V), the 20th harmonic in the output current of each inverter will be significantly affected. The distortion rate of 20th current harmonic of each inverter increases by 0.468%, so the amplitudes of $\triangle i_{ga1\_20}/\triangle u_{ga\_20}$ and $\triangle i_{ga2\_20}/\triangle u_{ga\_20}$ are both 0.0946, and the amplitude of $\triangle i_{sa\_20}/\triangle u_{ga\_20}$ is 0.1892. In the case of the carrier phase difference of 120° between the two inverters, when the grid voltage is ideal, with 5% 7th harmonic and 5% 20th harmonic, the output waveforms of the two inverters and the total grid-connected current are shown in Fig. 12, and the corresponding FFT analysis is shown in Fig. 13. When there are 7th and 20th harmonics in the grid voltage, the 7th and 20th harmonics in the output current of each inverter will be significantly affected. When the content of 7th harmonic

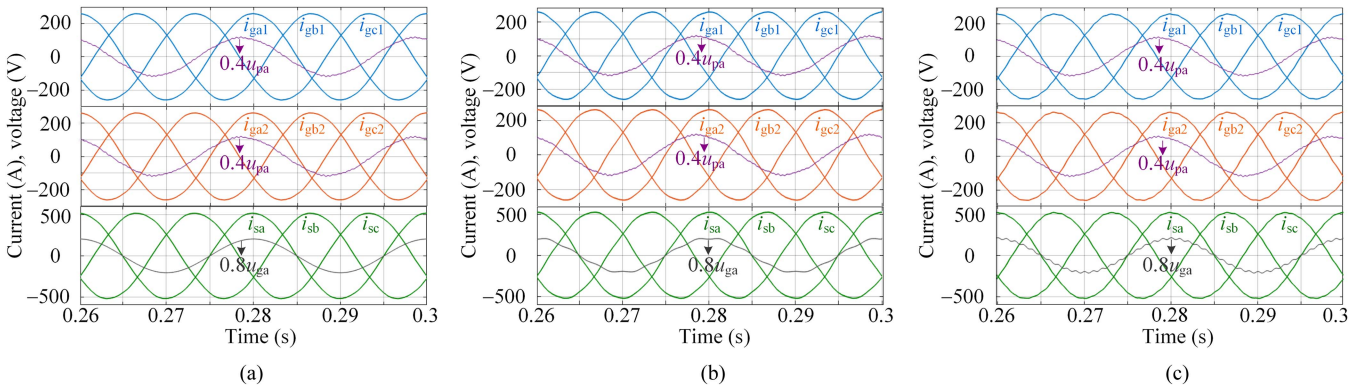

Fig. 10. Output waveforms of two inverters and total grid-connected current under synchronous carriers. (a) Ideal grid. (b) Inject 5% 7th harmonic into grid. (c) Inject 5% 20th harmonic into grid.

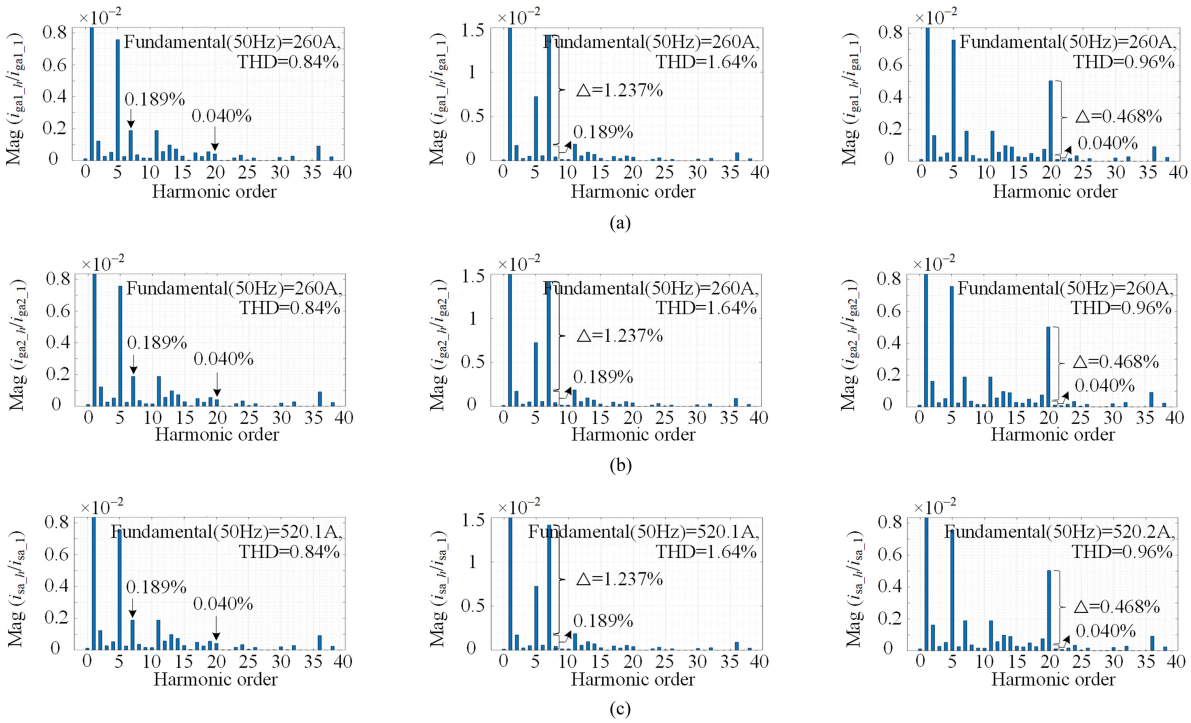

Fig. 11. FFT analysis of inverter output current under synchronous carriers. (a) i_{ga1}. (b) i_{ga2}. (c) i_{sa}. (In each figure, left: ideal grid, medium: inject 5% 7th harmonic into grid, right: inject 5% 20th harmonic into grid.)

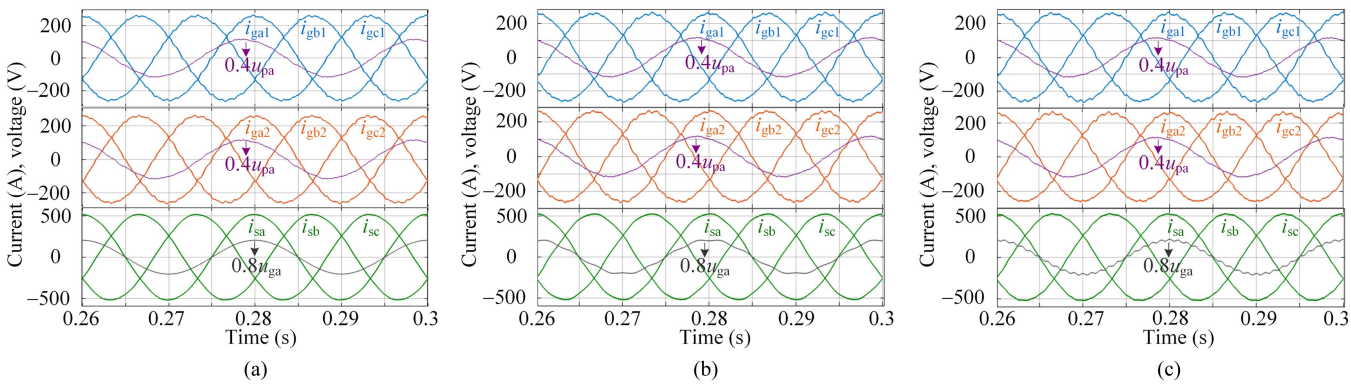

Fig. 12. Output waveforms of two inverters and total grid-connected current when the carrier phase difference is 120°. (a) Ideal grid. (b) Inject 5% 7th harmonic into grid. (c) Inject 5% 20th harmonic into grid.

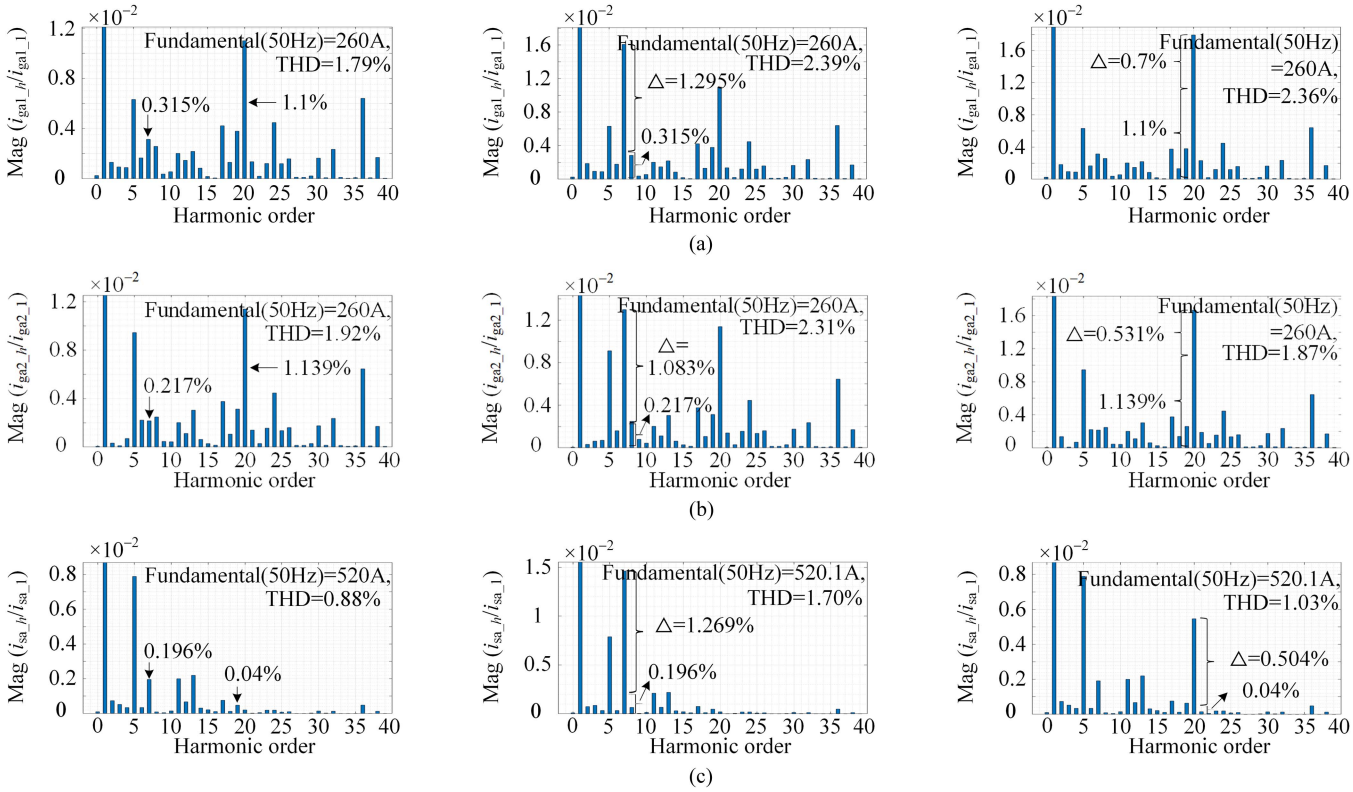

Fig. 13. FFT analysis of inverter output current when the carrier phase difference is 120°. (a) i_{ga1}. (b) i_{ga2}. (c) i_{sa}. (In each figure, left: ideal grid, medium: inject 5% 7th harmonic into grid, right: inject 5% 20th harmonic into grid.)

in the grid is 5% ($u_{\mathrm{ga\_7\_peak}} = 12.85$ V), the distortion rate of 7th harmonic in each inverter and in total grid-connected current increases by 1.295%, 1.083%, and 1.269%, respectively. So, the amplitudes of $\triangle i_{\mathrm{ga1\_7}}/\triangle u_{\mathrm{ga\_7}}$, $\triangle i_{\mathrm{ga2\_7}}/\triangle u_{\mathrm{ga\_7}}$, and $\triangle i_{\mathrm{sa\_7}}/\triangle u_{\mathrm{ga\_7}}$ are 0.2479, 0.2191, and 0.5134, respectively. When the content of 20th harmonic in the grid is 5% ($u_{\mathrm{ga\_20\_peak}} = 12.85$ V), the distortion rate of 20th harmonic in each inverter and in total grid-connected current increases by 0.7%, 0.531%, and 0.504%, respectively. So, we can obtain the amplitudes of $\triangle i_{\mathrm{ga1\_20}}/\triangle u_{\mathrm{ga\_20}}$, $\triangle i_{\mathrm{ga2\_20}}/\triangle u_{\mathrm{ga\_20}}$, and $\triangle i_{\mathrm{sa\_20}}/\triangle u_{\mathrm{ga\_20}}$ are 0.1416, 0.1074, and 0.2038, respectively. It can be seen, the model analysis results shown in Fig. 7 are basically consistent with the circuit simulation results mentioned earlier.

B. Frequency-Domain Analysis and Verification Under Parallel System Parameter II

The frequency domain analysis and validation process under system parameter II is similar to that under system parameter I. Therefore, this subsection will show and briefly explain the relevant analysis results, and the relevant figures and charts are detailed in Appendix B.

1) Characteristic Analysis of Grid Voltage to Output Current:

a) Coupling analysis of grid voltage to output current: Under system parameter II, when the carriers of the two inverters are synchronous and the carrier phase difference is 120°, taking phase a as an example, the harmonic coupling diagrams of $i_{\mathrm{ga1\_}h\mathrm{o}}/u_{\mathrm{ga\_}h\mathrm{i}}$, $i_{\mathrm{ga2\_}h\mathrm{o}}/u_{\mathrm{ga\_}h\mathrm{i}}$, and $i_{\mathrm{sa\_}h\mathrm{o}}/u_{\mathrm{ga\_}h\mathrm{i}}$ are shown in Figs. 22 and 23. It can be considered that regardless of whether the carriers are synchronous or not, the harmonics in the grid only affect the output current components of inverter with the same frequency.

b) Gain analysis of uncoupled terms for grid voltage to output current: The gain diagrams of uncoupled terms between the grid voltage and the output current under synchronous carriers are shown in Fig. 24(a) of Appendix B. $i_{\mathrm{ga1\_}h}/u_{\mathrm{ga\_}h}$ and $i_{\mathrm{ga2\_}h}/u_{\mathrm{ga\_}h}$ are identical, and the uncoupled gain between the grid voltage and the total grid-connected current is twice the corresponding gain of the single inverter. When the carrier phase difference between the two inverters is 120°, the gain diagrams of uncoupled terms between the grid voltage and output current are shown in Fig. 24(b). Comparing Fig. 24(b) with Fig. 24(a), there are slight differences in mid- and low-frequency gains (7th–24th) of the uncoupled terms between the grid voltage and output current. In addition, comparing $i_{\mathrm{ga1\_}h}/u_{\mathrm{ga\_}h}$ and $i_{\mathrm{ga2\_}h}/u_{\mathrm{ga\_}h}$ in Fig. 24(b), there are also differences in mid- and low-frequency characteristics (6th–14th, 18th–26th) between the grid voltage and output current of the two inverters under asynchronous carriers. The mechanism that produces the above-mentioned phenomenon has been detailed in Section IV-A-1)-b) and will not be repeated here.

Relevant conclusions are similar to those in Section IV-A-1)-b). Section IV-B-3) will illustrate the accuracy of the HSS model constructed under system parameter II by comparing with the circuit simulation results.

2) Characteristic Analysis of Current Reference to Output Current: When the carriers are synchronized, the pole maps between the current reference and the output current of the two inverters are shown in Fig. 25 of Appendix B. It is obvious, the parallel system is stable under system parameter II, and the harmonic stability of the two inverters is completely consistent under synchronous carriers. When the carrier phase difference between two inverters is 120°, the pole maps between the current reference and the output current of the two inverters are shown in Fig. 26. Through data comparison, the positions of all central poles in Figs. 25 and 26 are completely consistent. However, the mid-frequency pole position near the 20th, namely the part marked by a black circle, is significantly different from that under synchronous carriers; while the low- and high-frequency pole positions are similar to that under synchronous carriers. Relevant conclusions are similar to those in Section IV-A-2).

3) Circuit Simulation Verification: Simulink circuit simulation analysis is carried out, to finish the accuracy verification of the complete HSS model of the parallel system proposed in Section III-A under system parameter II.

In the case of carrier synchronization between two inverters, when the grid voltage is ideal, with 5% 7th harmonic and 5% 20th harmonic, the output waveforms of the two inverters and the total grid-connected current are shown in Fig. 27, and the corresponding FFT analysis is shown in Fig. 28. When the carriers are synchronized, the above-mentioned circuit simulation results show that the harmonic characteristics of the two inverters are completely consistent, this is consistent with the analysis results of Sections IV-B-1 and IV-B-2. In addition, when there is 5% 7th harmonic in the grid voltage ($u_{\mathrm{ga\_7\_peak}} = 0.707$ V), the distortion rate of 7th current harmonic of each inverter increases by 0.274%, so the amplitudes of $\triangle i_{\mathrm{ga1\_7}}/\triangle u_{\mathrm{ga\_7}}$ and $\triangle i_{\mathrm{ga2\_7}}/\triangle u_{\mathrm{ga\_7}}$ are both 0.0232, and the amplitude of $\triangle i_{\mathrm{sa\_7}}/\triangle u_{\mathrm{ga\_7}}$ is 0.0464. Similarly, when there is 5% 20th harmonic in the grid voltage ($u_{\mathrm{ga\_20\_peak}} = 0.707$ V), the distortion rate of 20th current harmonic of each inverter increases by 0.773%, so the amplitudes of $\triangle i_{\mathrm{ga1\_20}}/\triangle u_{\mathrm{ga\_20}}$ and $\triangle i_{\mathrm{ga2\_20}}/\triangle u_{\mathrm{ga\_20}}$ are both 0.0656, and the amplitude of $\triangle i_{\mathrm{sa\_20}}/\triangle u_{\mathrm{ga\_20}}$ is 0.1312. In the case of the carrier phase difference of 120° between the two inverters, when the grid voltage is ideal, with 5% 7th harmonic and 5% 20th harmonic, the output waveforms of the two inverters and the total grid-connected current are shown in Fig. 29, and the corresponding FFT analysis is shown in Fig. 30. Comparing Figs. 28 and 30, after the carriers are out of synchronization, the mid-frequency harmonic characteristics of the output current of the two inverters will change significantly. This phenomenon in circuit simulation indirectly confirms the rationality of the model analysis results in Sections IV-B-1) and IV-B-2). In addition, when there are 7th and 20th harmonics in the grid voltage, the 7th and 20th harmonics in the output current of each inverter will be significantly affected. When the content of 7th harmonic in the grid is 5% ($u_{\mathrm{ga\_7\_peak}} = 0.707$ V), the distortion rate of 7th harmonic in each inverter and in total grid-connected current increases by 0.304%, 0.122%, and 0.205%, respectively. So, the amplitudes of $\triangle i_{\mathrm{ga1\_7}}/\triangle u_{\mathrm{ga\_7}}$, $\triangle i_{\mathrm{ga2\_7}}/\triangle u_{\mathrm{ga\_7}}$, and $\triangle i_{\mathrm{sa\_7}}/\triangle u_{\mathrm{ga\_7}}$ are 0.0258, 0.0104, and 0.0347, respectively. When the content of 20th harmonic in the grid is 5% ($u_{\mathrm{ga\_20\_peak}} = 0.707$ V), the distortion rate of 20th harmonic in each inverter and in total grid-connected current increases by 0.565%, 0.781%, and 0.747%, respectively. So, the amplitudes of $\triangle i_{\mathrm{ga1\_20}}/\triangle u_{\mathrm{ga\_20}}$, $\triangle i_{\mathrm{ga2\_20}}/\triangle u_{\mathrm{ga\_20}}$, and $\triangle i_{\mathrm{sa\_20}}/\triangle u_{\mathrm{ga\_20}}$ are 0.0479, 0.0662, and 0.1267, respectively. It can be seen, the model analysis results shown in Fig. 24 are basically consistent with the circuit simulation results mentioned earlier.

V. Accuracy Verification of Iterative Calculation Method for Parallel-System HSS Model

Under two groups of system parameters, this section will verify the accuracy of the iterative calculation method for the parallel-system HSS model considering asynchronous carriers proposed in Section III-B.

A. Accuracy Verification of Iterative Calculation Method Under System Parameter I

When the carrier phase difference is 120°, taking the fundamental, 7th and 20th grid-side current components as examples, the dynamic waveforms of the output current amplitude and phase obtained through the iterative calculation method of the parallel-system HSS model proposed in this article are shown in Fig. 14. Meanwhile, this subsection summarizes the steady-state values of the amplitude and phase of the main harmonic components in the output current calculated by the model, and compares them with the circuit simulation results, as shown in Table III. After analysis, the maximum deviation rate between the model calculation results of the current amplitude and the circuit simulation results is 10%, and the maximum deviation of the phase is 16°. Although there are some differences between the model calculation results and the circuit simulation results, overall, the above-mentioned results indicate that the parallel-system HSS model constructed in this article is correct. Meanwhile, the proposed iterative calculation method for parallel-system HSS model has high accuracy under system parameter I.

B. Accuracy Verification of Iterative Calculation Method Under System Parameter II

When the carrier phase difference is 120°, taking the fundamental, 7th and 24th grid-side current components as examples, the dynamic waveforms of the current amplitude and phase are shown in Fig. 31. The steady-state values of the amplitude and phase of the main current components obtained through model calculation and circuit simulation are shown in Table IV. Under system parameter II, due to the low voltage and current levels, the amplitude of some harmonics is too small, which leads to the significant errors between individual model calculation results and circuit simulation results. However, this situation is understandable, and overall, the errors in most model calculation results are within an acceptable range. Therefore, under system parameter II, the proposed iterative calculation method also has high accuracy.

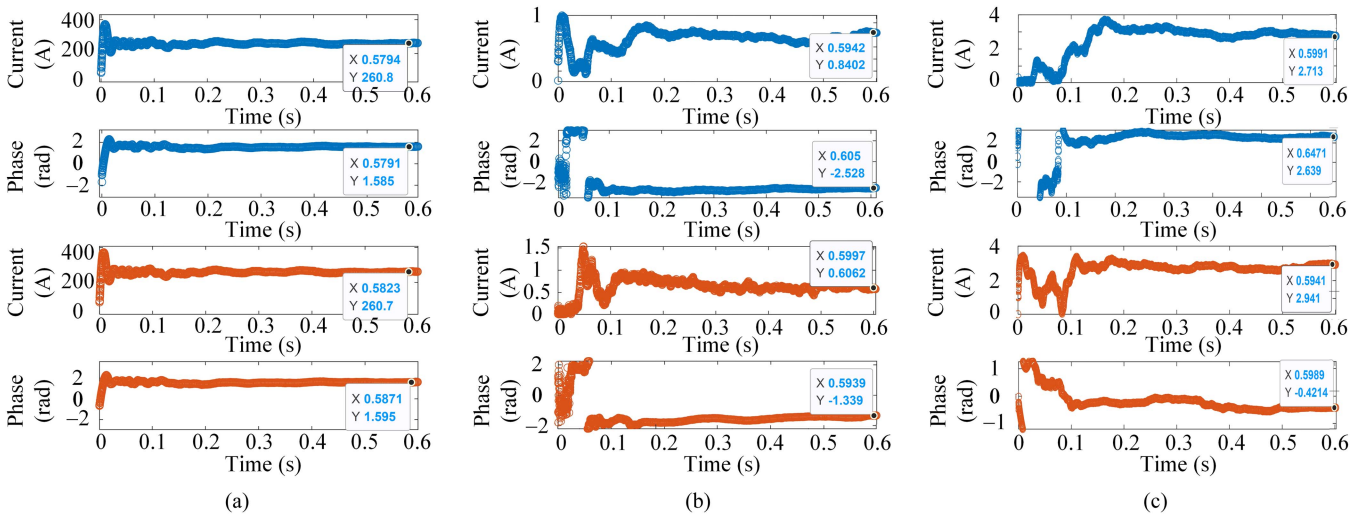

Fig. 14. Dynamic waveforms of output current amplitude and phase of two inverters with the carrier phase difference of 120°. (a) Fundamental component. (b) 7th harmonic component. (c) 20th harmonic component. (Blue: first inverter, orange: second inverter.)

TABLE III
COMPARISON TABLE BETWEEN MODEL CALCULATION RESULTS AND CIRCUIT SIMULATION RESULTS UNDER SYSTEM PARAMETER I

Current component order	First inverter output current $i_{ga1\ h}$				Second inverter output current $i_{ga2\ h}$			
	Model calculation results		Circuit simulation results		Model calculation results		Circuit simulation results	
	Amplitude/A	Phase/rad	Amplitude/A	Phase/rad	Amplitude/A	Phase/rad	Amplitude/A	Phase/rad
1	260.8	1.585	260	1.57	260.7	1.595	260	1.57
5	1.586	3.304	1.64	3.11	2.575	2.837	2.46	3.11
7	0.8402	-2.528	0.82	-2.65	0.6061	-1.339	0.56	-1.13
11	0.4991	0.2775	0.53	0.28	0.5006	0.1086	0.53	-0.03
13	0.5216	-2.908	0.57	-3.04	0.8552	-1.691	0.79	-1.87
20	2.713	2.639	2.86	2.72	2.941	-0.4214	2.96	-0.42
24	1.100	-2.883	1.17	-2.67	1.298	0.51	1.16	0.56
32	0.5921	2.063	0.61	1.97	0.7188	-1.182	0.62	-1.04
36	1.604	-2.111	1.67	-2.06	1.596	1.094	1.68	1.22
38	0.4471	-1.057	0.44	-0.84	0.4322	2.593	0.44	2.46

VI. EXPERIMENTAL VERIFICATION

A parallel experimental platform for two three-level *LCL* GCIs based on the GCF PI+CCF AD control strategy is built, to further verify the accuracy of the model proposed in this article and the correctness of the frequency-domain analysis results. The inverter parallel experimental platform is shown in Fig. 15. In the experiment, two dc power supplies IT6525D provided dc bus voltage to the two inverters, and the CSW5550 programmable ac power supply is used to simulate the grid. Each inverter uses DSP+FPGA to complete the control functions. Among them, the XC6SLX25 FPGA produced by Xilinx Company is used to realize the functions of PD-PWM signal generation, signal sampling, and so on. The DSP with the model TMS320C28346 produced by Texas Instruments is used to realize coordinate transformation, current closed-loop control, and so on. The experimental parameters are shown in Table II. The accuracy of the proposed model and frequency-domain analysis results will be verified through the following experiments.

First, relevant experiments are conducted under the synchronous carriers. The output current of phase a in two inverters,

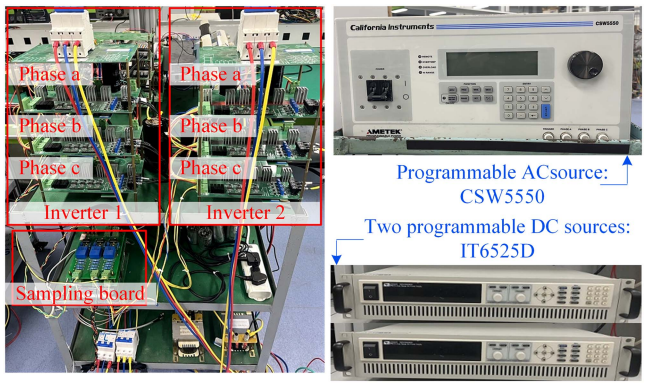

Fig. 15. Three-level *LCL* GCI parallel experimental platform.

the total grid-connected current of phase a, and the corresponding FFT analysis are shown in Fig. 16. From the FFT analysis, the harmonic characteristics of the two inverters are almost identical. Figs. 17 and 18 show the waveforms and FFT analysis results after injecting 5% 7th harmonic and 5% 20th harmonic into grid under the synchronous carriers. It can be seen, even if the grid

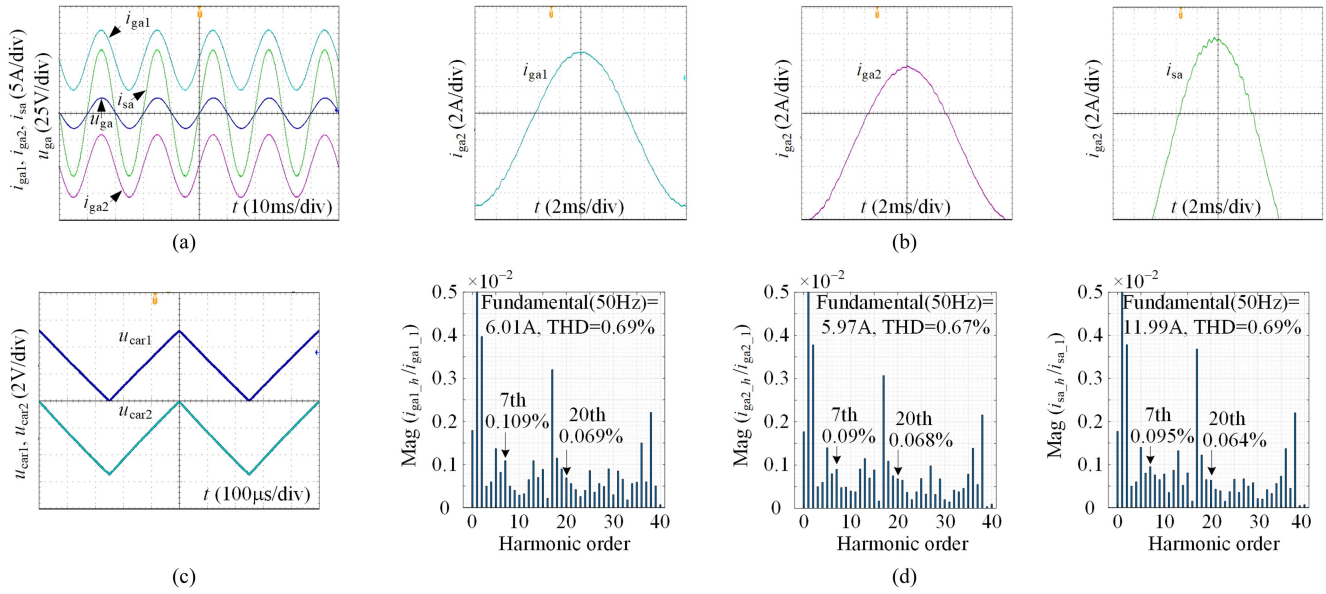

Fig. 16. Output current waveforms and FFT analysis of parallel system when the carriers are synchronized and the grid is ideal. (a) i_{ga1}, i_{ga2}, i_{sa}, and u_{ga}. (b) Enlarged waveforms of i_{ga1}, i_{ga2}, and i_{sa}. (c) Carriers. (d) FFT analysis.

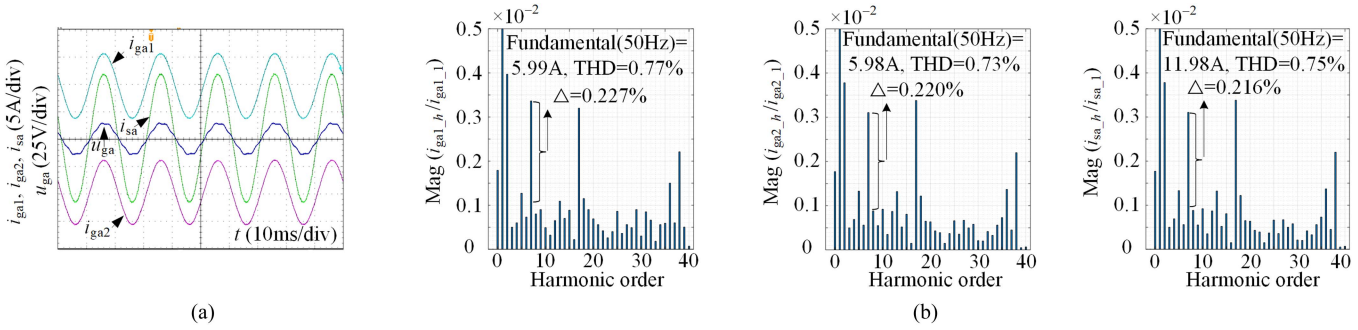

Fig. 17. Output current waveforms and FFT analysis of parallel system when the carriers are synchronized and the grid contains 5% 7th harmonic. (a) i_{ga1}, i_{ga2}, i_{sa}, and u_{ga}. (b) FFT analysis.

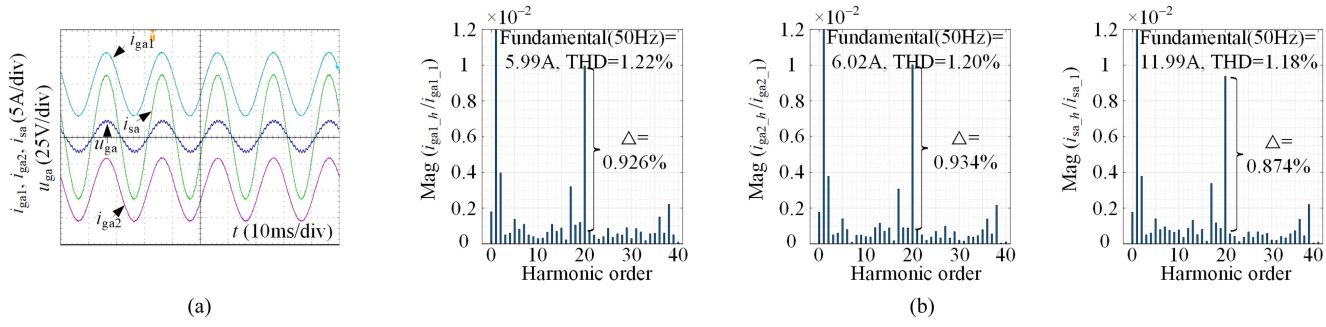

Fig. 18. Output current waveforms and FFT analysis of parallel system when the carriers are synchronized and the grid contains 5% 20th harmonic. (a) i_{ga1}, i_{ga2}, i_{sa}, and u_{ga}. (b) FFT analysis.

conditions change, as long as the carriers are always synchronized, the harmonic characteristics of the output current of the two inverters are always basically the same. This is consistent with the model analysis results in Section IV-B. In addition, the 7th or 20th grid harmonics, will mainly have the significant impact on the same frequency harmonic components in the output current. After measurement, when injecting 5% 7th harmonic into grid ($u_{ga\_7\_peak} = 0.707$ V), the distortion rate of 7th harmonic in each inverter output current and total grid-connected current basically increases by 0.22%. So, $\triangle i_{ga1\_7}/\triangle u_{ga\_7}$ and $\triangle i_{ga2\_7}/\triangle u_{ga\_7}$ are approximately 0.0190, and $\triangle i_{sa\_7}/\triangle u_{ga\_7}$ can be calculated to be approximately 0.0366. When injecting 5% 20th harmonic into grid ($u_{ga\_20\_peak} = 0.707$ V), the distortion rate of 20th harmonic in each inverter output current

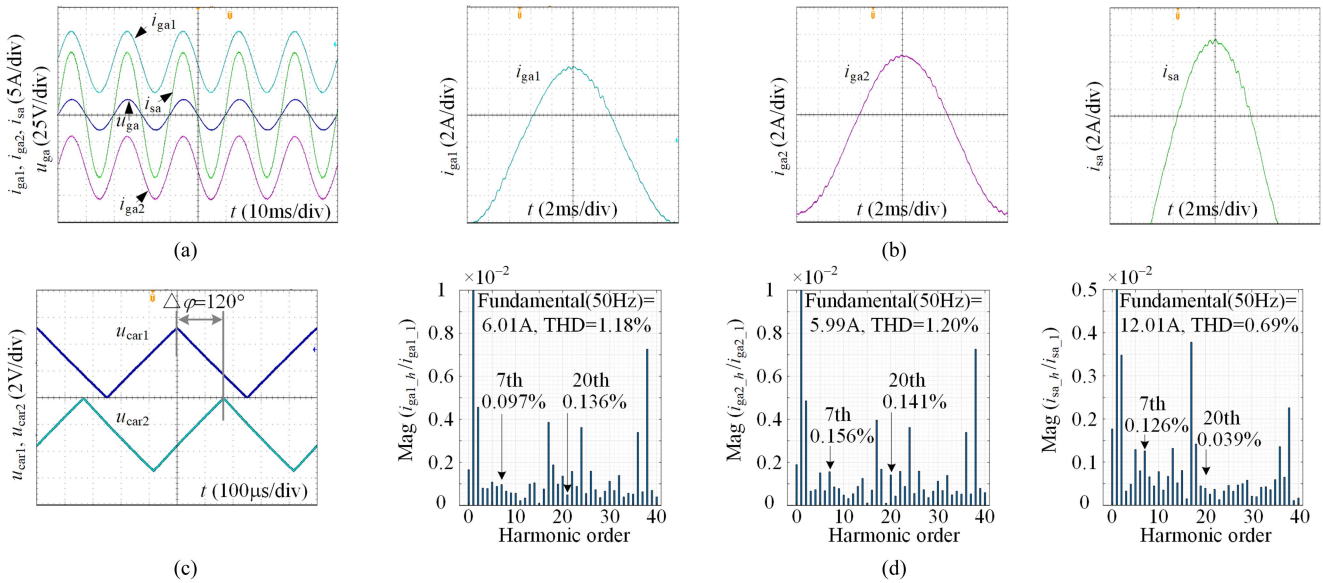

Fig. 19. Output current waveforms and FFT analysis of parallel system when the carrier phase difference is 120° and the grid is ideal. (a) i_{ga1}, i_{ga2}, i_{sa}, and u_{ga}. (b) Enlarged waveforms of i_{ga1}, i_{ga2}, and i_{sa}. (c) Carriers. (d) FFT analysis.

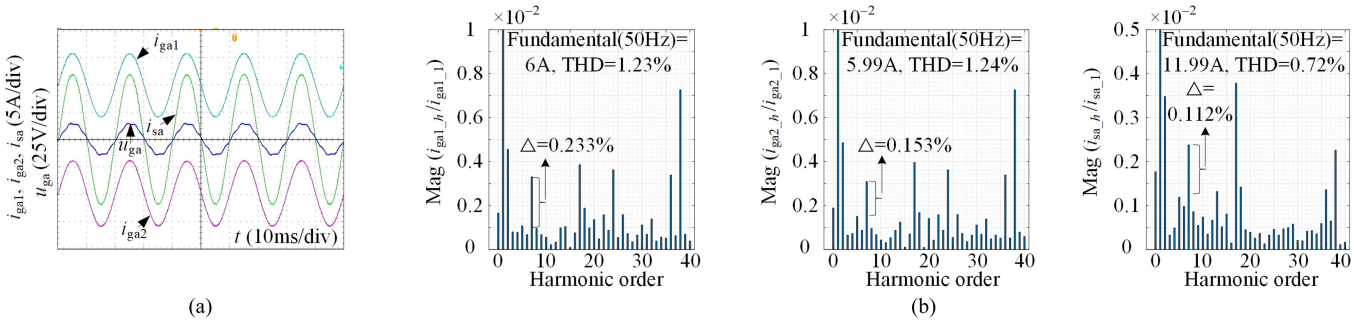

Fig. 20. Output current waveforms and FFT analysis of parallel system when the carrier phase difference is 120° and the grid contains 5% 7th harmonic. (a) i_{ga1}, i_{ga2}, i_{sa}, and u_{ga}. (b) FFT analysis.

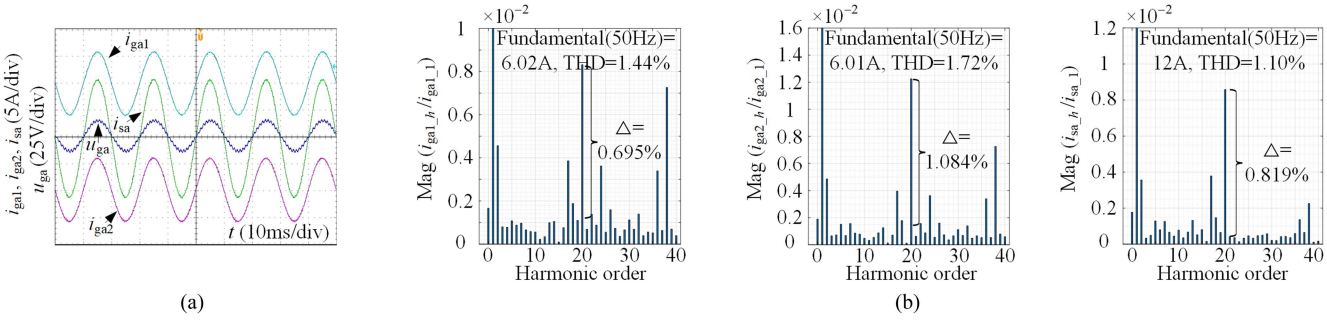

Fig. 21. Output current waveforms and FFT analysis of parallel system when the carrier phase difference is 120° and the grid contains 5% 20th harmonic. (a) i_{ga1}, i_{ga2}, i_{sa}, and u_{ga}. (b) FFT analysis.

and total grid-connected current basically increases by 0.93%. So, $\triangle i_{ga1\_20}/\triangle u_{ga\_20}$ and $\triangle i_{ga2\_20}/\triangle u_{ga\_20}$ are approximately 0.079, and $\triangle i_{sa\_20}/\triangle u_{ga\_20}$ can be calculated to be approximately 0.1484.

Second, relevant experiments are conducted with the carrier phase difference of 120°. The output current of phase a in two inverters, the total grid-connected current of phase a, and FFT analysis are shown in Fig. 19. Compared with the case of carrier synchronization, the mid- and high-frequency harmonic contents of the output current of the two inverters change under asynchronous carriers. This is consistent with the model calculation results and circuit simulation phenomena. Figs. 20 and 21show the waveforms and FFT analysis results after injecting 5% 7th harmonic and 5% 20th harmonic into grid under the

asynchronous carriers. It can be seen, the grid harmonics will also mainly affect the same frequency harmonic components in the output current. When there is 5% 7th harmonic in the grid voltage ($u_{\mathrm{ga\_7\_peak}} = 0.707$ V), the distortion rate of 7th harmonic in each inverter output current and total grid-connected current increases by 0.233%, 0.153%, and 0.112%, respectively. So, the amplitudes of $\triangle i_{\mathrm{ga1\_7}}/\triangle u_{\mathrm{ga\_7}}$, $\triangle i_{\mathrm{ga2\_7}}/\triangle u_{\mathrm{ga\_7}}$, and $\triangle i_{\mathrm{sa\_7}}/\triangle u_{\mathrm{ga\_7}}$ are 0.0198, 0.013, and 0.019, respectively. When there is 5% 20th harmonic in the grid voltage ($u_{\mathrm{ga\_20\_peak}} = 0.707$ V), the distortion rate of 20th harmonic in each inverter output current and total grid-connected current increases by 0.695%, 1.08%, and 0.819%, respectively. So, the amplitudes of $\triangle i_{\mathrm{ga1\_20}}/\triangle u_{\mathrm{ga\_20}}$, $\triangle i_{\mathrm{ga2\_20}}/\triangle u_{\mathrm{ga\_20}}$, and $\triangle i_{\mathrm{sa\_20}}/\triangle u_{\mathrm{ga\_20}}$ are 0.059, 0.092, and 0.139, respectively.

Although there are some errors between the experimental data and the model analysis results in Fig. 24, if nonideal factors in the experiment are ignored, it can be considered, the model analysis results in Fig. 24 can basically reflect the harmonic characteristics of the actual parallel system. This indicates that the complete HSS model of the inverter parallel system proposed in Section III-A is effective and accurate.

VII. Discussion on the Extension of Proposed Methods in Parallel System of *N* Inverters

The methods proposed in this article are applicable to the parallel system of *n* inverters ($n \geq 2$).

1) A general construction method for parallel-system complete HSS model of *n* inverters considering asynchronous carriers (refer to Section III-A):
   a) Construct the LTP model of *n* GCIs considering digitization impact;
   b) Construct the PCC LTP model containing *n* inverters;
   c) Reconstruct and integrate the LTP models of the above-mentioned parts into a whole;
   d) Convert the parallel-system complete LTP model into the parallel-system complete HSS model. It should be noted, when the carrier phase of each inverter is different, the Toeplitz matrix of the switching function of each inverter is also different.
2) A general iterative-calculation method for parallel-system HSS model of *n* inverters considering asynchronous carriers (refer to Section III-B):
   a) Construct and calculate the HSS models of the respective controllers and main circuits of *n* inverters in sequence;
   b) Reproduce the PWM process of *n* inverters;
   c) Construct and calculate the PCC harmonic model containing *n* inverters. The implementation process is similar to Fig. 4.

VIII. Conclusion

This article takes the parallel system of two LSF *LCL* GCIs as an example, based on [12] and [13], conducts the research on the extension in parallel system of HSS modeling, harmonic calculation, and analysis methods for the single *LCL* GCI. The main conclusions are as follows.

1) The proposed complete-HSS-model for parallel system considering asynchronous carriers is effective, and the analysis results based on this model can accurately reflect the impact of asynchronous carriers on system characteristics.
2) The model analysis results indicate: asynchronous carriers can affect the mid-frequency harmonic stability of the output current of each inverter in parallel system; and also affect the mid-frequency antidistarbance characteristic of the output current of each inverter to the grid voltage.
3) The proposed iterative-calculation method of parallel-system HSS model considering asynchronous carriers is feasible, and achieves efficient and accurate calculation of the harmonic amplitude and phase of the output current of each inverter and the total grid-connected current.

The related research involved in this article fills the gap in harmonic-domain modeling and analysis of parallel system under asynchronous carriers, and provides certain theoretical support for related research.

Appendix A

$$\boldsymbol{A}_{\mathrm{pt}}(t) = \begin{bmatrix} \boldsymbol{A}_{\mathrm{p1}}(t) & \\ & \boldsymbol{A}_{\mathrm{p2}}(t) \end{bmatrix},$$

$$\boldsymbol{C}_{\mathrm{pt}}(t) = \begin{bmatrix} \boldsymbol{C}_{\mathrm{s1}}(t) & \boldsymbol{Z}_{3\times14} \\ \boldsymbol{Z}_{3\times14} & \boldsymbol{C}_{\mathrm{s2}}(t) \end{bmatrix} \tag{A1-1}$$

$$\boldsymbol{B}_{\mathrm{pt}}(t) = \begin{bmatrix} \boldsymbol{B}_{\mathrm{p1}}(t)_{(c1\sim c3)} & \boldsymbol{Z}_{14\times3} & \boldsymbol{B}_{\mathrm{p1}}(t)_{(c4\sim c6)} \\ \boldsymbol{Z}_{14\times3} & \boldsymbol{B}_{\mathrm{p2}}(t)_{(c1\sim c3)} & \boldsymbol{B}_{\mathrm{p2}}(t)_{(c4\sim c6)} \end{bmatrix}. \tag{A1-2}$$

$$\boldsymbol{A}_{\mathrm{cp}}(t) = \begin{bmatrix} \boldsymbol{A}_{\mathrm{pt}}(t) & \boldsymbol{Z}_{28\times3} \end{bmatrix},\ \boldsymbol{C}_{\mathrm{cp}}(t) = \begin{bmatrix} \boldsymbol{C}_{\mathrm{pt}}(t) & \boldsymbol{Z}_{6\times3} \end{bmatrix}. \tag{A2}$$

$$\boldsymbol{M}_{\mathrm{cp}}(t) = \begin{bmatrix} \multicolumn{6}{c}{\boldsymbol{Z}_{6\times31}} \\ \hdashline \boldsymbol{Z}_{3\times3} & R_V\boldsymbol{I}_3 & \boldsymbol{Z}_{3\times11} & R_V\boldsymbol{I}_3 & \boldsymbol{Z}_{3\times8} & -R_V\boldsymbol{I}_3 \end{bmatrix}, \tag{A3-1}$$

$$\boldsymbol{N}_{\mathrm{cp}}(t) = \begin{bmatrix} \boldsymbol{I}_3 & \boldsymbol{Z}_{3\times3} & \boldsymbol{Z}_{3\times3} \\ \boldsymbol{Z}_{3\times3} & \boldsymbol{I}_3 & \boldsymbol{Z}_{3\times3} \\ \boldsymbol{Z}_{3\times3} & \boldsymbol{Z}_{3\times3} & \boldsymbol{Z}_{3\times3} \end{bmatrix}. \tag{A3-2}$$

$$\boldsymbol{O}_{\mathrm{cp}}(t) = \begin{bmatrix} \boldsymbol{Z}_{3\times3} & \frac{R_{\mathrm{V}}}{L_{\mathrm{g}}}\boldsymbol{I}_3 & \boldsymbol{Z}_{3\times11} & \frac{R_{\mathrm{V}}}{L_{\mathrm{g}}}\boldsymbol{I}_3 & \boldsymbol{Z}_{3\times8} & -\frac{R_{\mathrm{V}}}{L_{\mathrm{g}}}\boldsymbol{I}_3 \end{bmatrix} \tag{A4-1}$$

$$\boldsymbol{P}_{\mathrm{cp}}(t) = \begin{bmatrix} \boldsymbol{Z}_{3\times6} & -\frac{1}{L_{\mathrm{g}}}\boldsymbol{I}_3 \end{bmatrix}. \tag{A4-2}$$

Wherein, the subscripts ($c1$–$c3$) and ($c4$–$c6$) represent the 1st–3rd columns and 4th–6th columns of the matrix, respectively. $Z_{\mathrm{m\times n}}$ represents the zero matrix of ($m\times n$), I_{e} represents the identity matrix of *e* dimension.

APPENDIX B

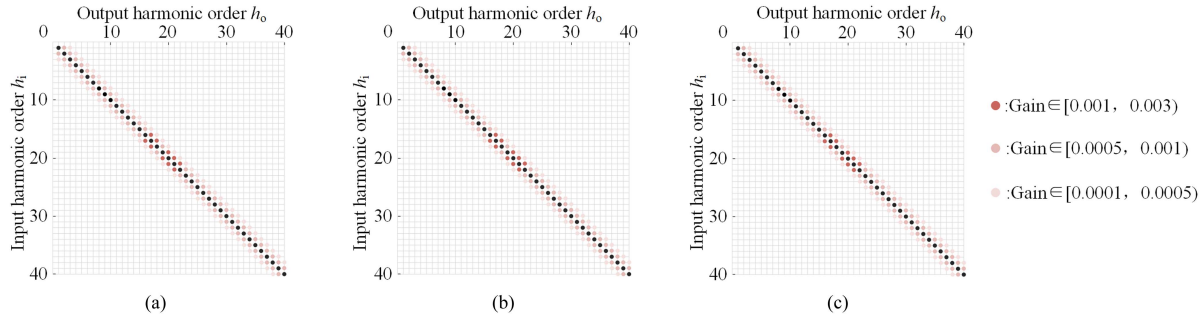

Fig. 22. Schematic diagrams of harmonic coupling between grid voltage and output current under synchronous carriers. (a) i_{ga1_ho}/u_{ga_hi}. (b) i_{ga2_ho}/u_{ga_hi}. (c) i_{sa_ho}/u_{ga_hi}.

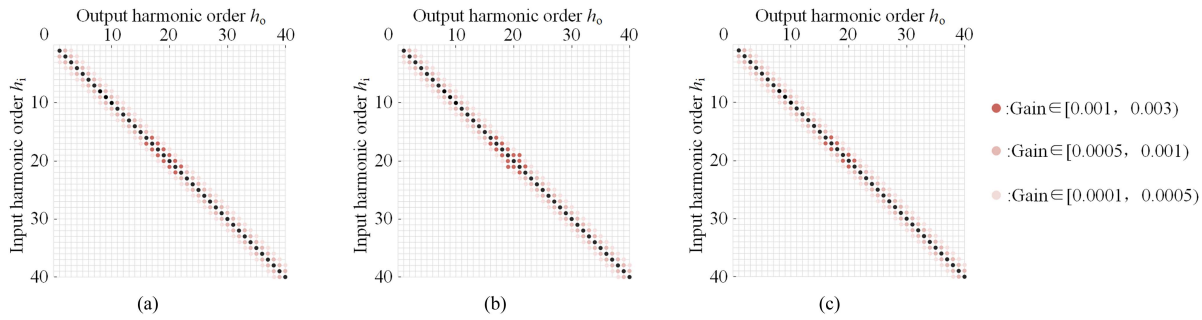

Fig. 23. Schematic diagrams of harmonic coupling between grid voltage and output current when the carrier phase difference is 120°. (a) i_{ga1_ho}/u_{ga_hi}. (b) i_{ga2_ho}/u_{ga_hi}. (c) i_{sa_ho}/u_{ga_hi}.

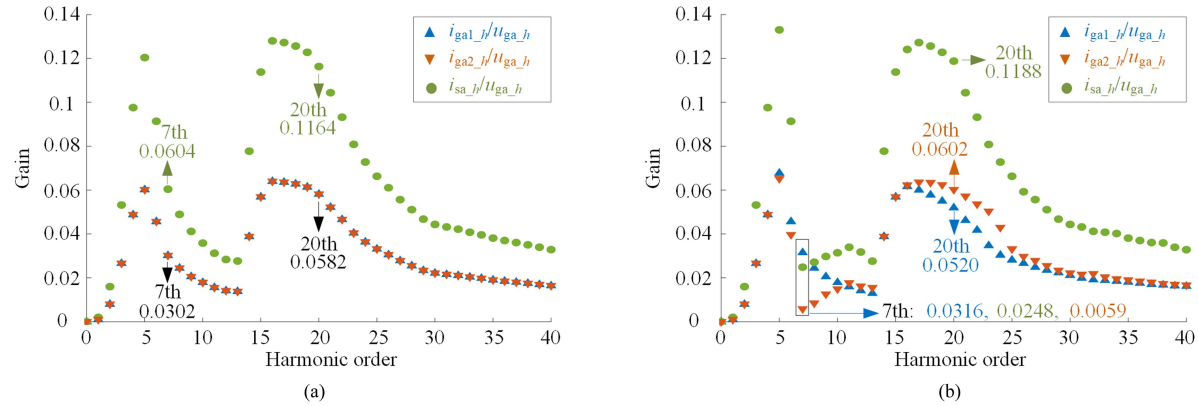

Fig. 24. Gain diagrams of uncoupled terms between grid voltage and output current. (a) Carrier synchronization. (b) Carrier phase difference of 120°.

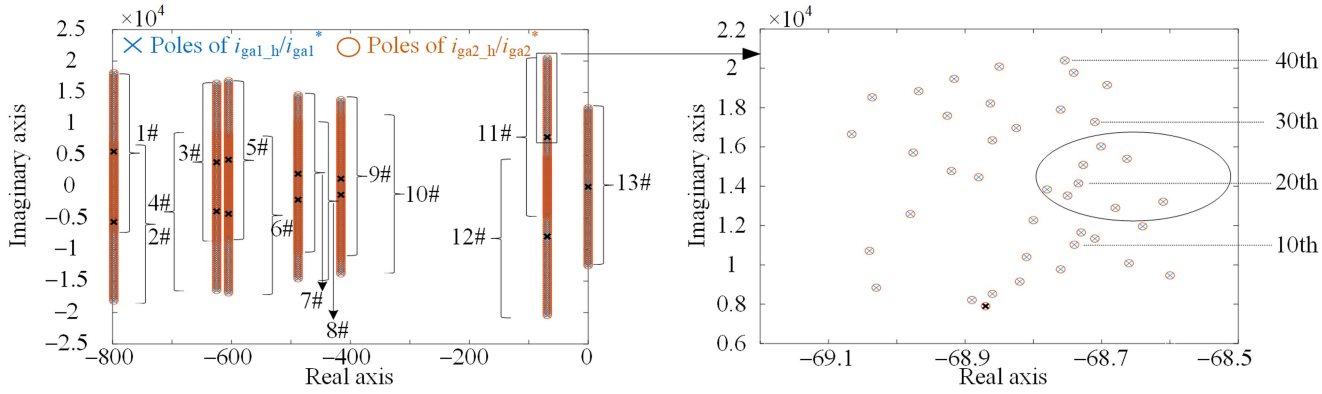

Fig. 25. Pole maps of i_{ga1_h}/i_{ga1}^* and i_{ga2_h}/i_{ga2}^* under synchronous carriers.

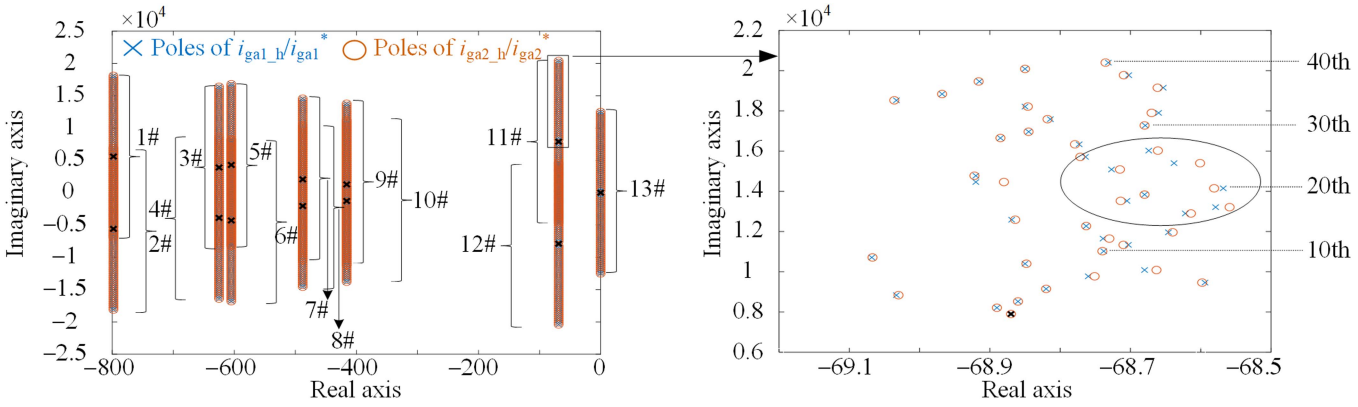

Fig. 26. Pole maps of i_{ga1_h}/i_{ga1}^* and i_{ga2_h}/i_{ga2}^* under asynchronous carriers.

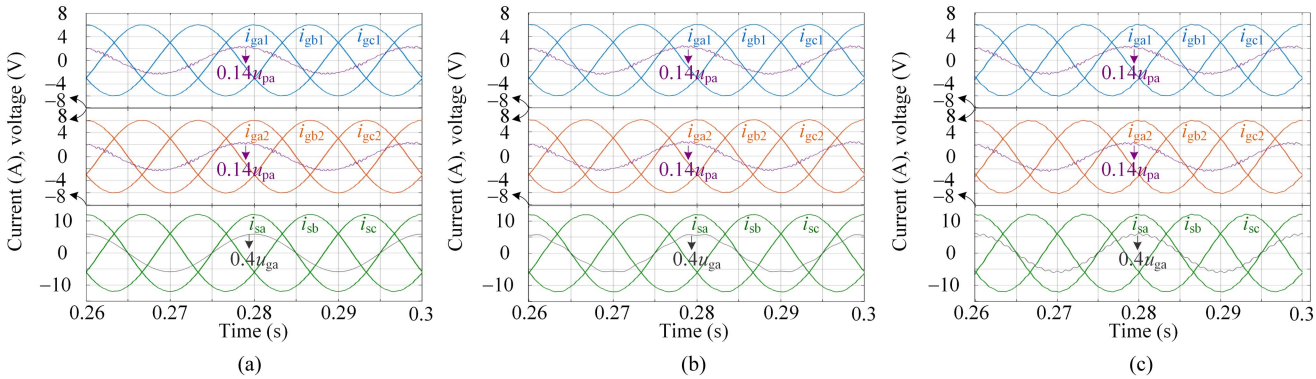

Fig. 27. Output waveforms of two inverters and total grid-connected current under synchronous carriers. (a) Ideal grid. (b) Inject 5% 7th harmonic into grid. (c) Inject 5% 20th harmonic into grid.

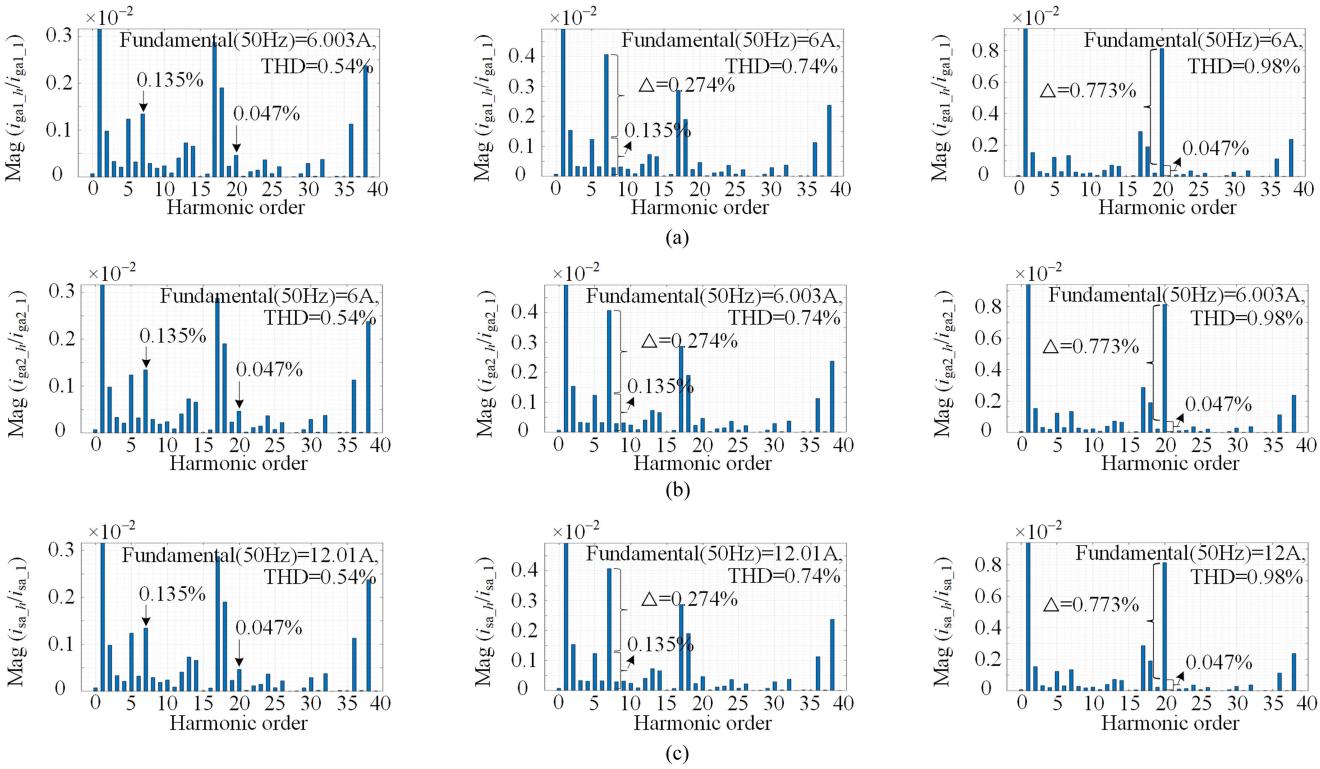

Fig. 28. FFT analysis of inverter output current under synchronous carriers. (a) i_{ga1}. (b) i_{ga2}. (c) i_{sa}. (In each figure, left: ideal grid, medium: inject 5% 7th harmonic into grid, right: inject 5% 20th harmonic into grid.).

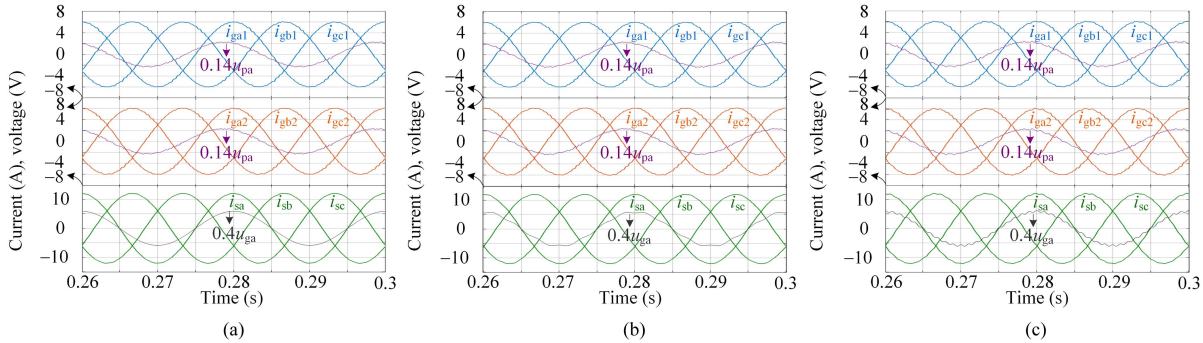

Fig. 29. Output waveforms of two inverters and total grid-connected current when the carrier phase difference is 120°. (a) Ideal grid. (b) Inject 5% 7th harmonic into grid. (c) Inject 5% 20th harmonic into grid.

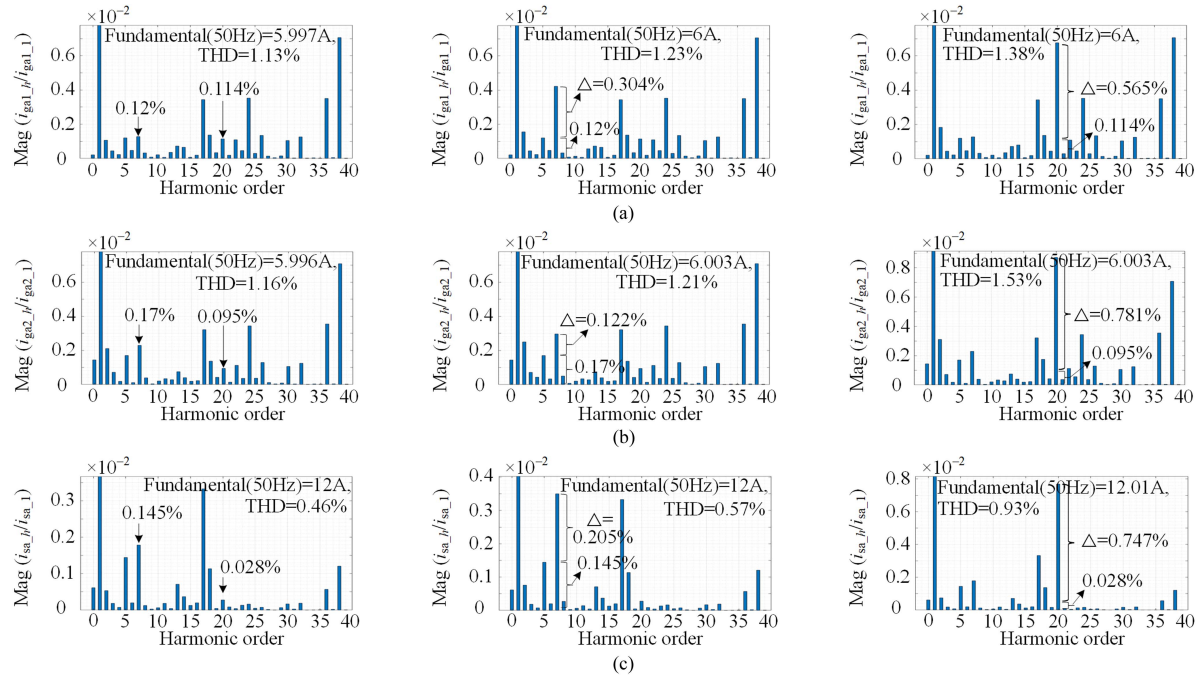

Fig. 30. FFT analysis of inverter output current when the carrier phase difference is 120°. (a) i_{ga1}. (b) i_{ga2}. (c) i_{sa}. (In each figure, left: ideal grid, medium: inject 5% 7th harmonic into grid, right: inject 5% 20th harmonic into grid.)

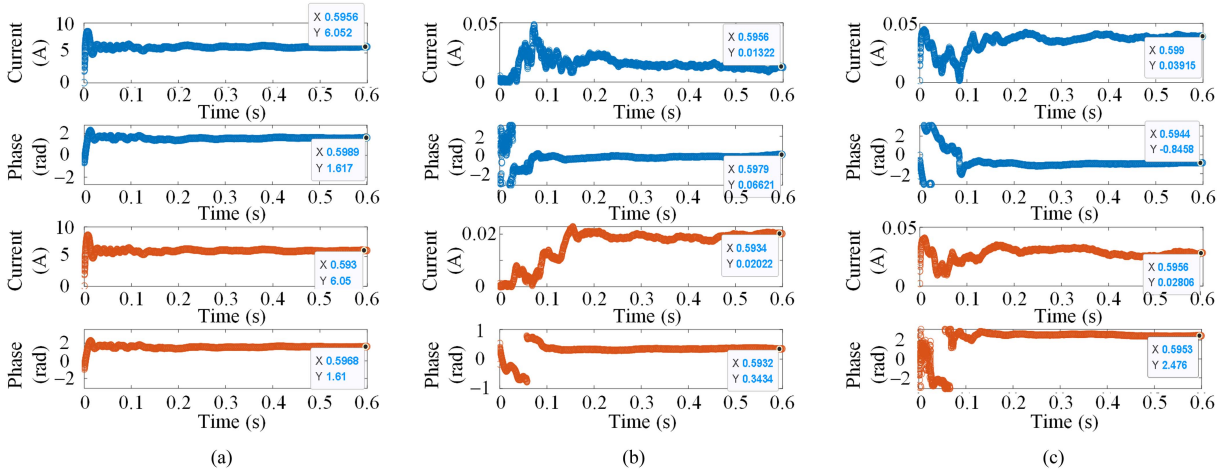

Fig. 31. Dynamic waveforms of output current amplitude and phase of two inverters with the carrier phase difference of 120°. (a) Fundamental component. (b) 7th harmonic component. (c) 24th harmonic component. (Blue: first inverter, orange: second inverter.)

TABLE IV
COMPARISON TABLE BETWEEN MODEL CALCULATION RESULTS AND CIRCUIT SIMULATION RESULTS UNDER SYSTEM PARAMETER II

Current component order	First inverter output current i_{ga1_h}				Second inverter output current i_{ga2_h}			
	Model calculation results		Circuit simulation results		Model calculation results		Circuit simulation results	
	Amplitude/A	Phase/rad	Amplitude/A	Phase/rad	Amplitude/A	Phase/rad	Amplitude/A	Phase/rad
1	6.052	1.617	6	1.57	6.05	1.610	6	1.57
5	0.01008	1.983	0.007	2.17	0.01369	2.076	0.010	2.35
7	0.01310	0.0662	0.007	-0.07	0.02022	0.3434	0.011	-0.09
11	0	/	0.001	2.37	0.001018	2.2735	0.002	2.37
13	0.002756	2.889	0.004	2.64	0.001295	2.262	0.004	2.09
20	0.01133	-0.3155	0.007	-0.35	0.01034	2.058	0.006	2.27
24	0.03915	-0.8458	0.021	-0.80	0.02806	2.476	0.020	2.43
32	0.009746	-0.3261	0.008	-0.28	0.005331	3.138	0.007	3.14
36	0.02088	-2.9887	0.021	-3.02	0.03719	0.0298	0.021	0.13
38	0.05273	1.5933	0.042	1.78	0.04993	0.04117	0.042	-1.03

REFERENCES

[1] J.-S. Kim, J.-M. Kwon, and B.-H. Kwon, "High-efficiency two-stage three-level grid-connected photovoltaic inverter," *IEEE Trans. Ind. Electron.*, vol. 65, no. 3, pp. 2368–2377, Mar. 2018.

[2] Y. Li, X. Yang, W. Chen, T. Liu, and F. Zhang, "Neutral-point voltage analysis and suppression for NPC three-level photovoltaic converter in LVRT operation under imbalanced grid faults with selective hybrid SVPWM strategy," *IEEE Trans. Power Electron.*, vol. 34, no. 2, pp. 1334–1355, Feb. 2019.

[3] Q. Yan, X. Wu, X. Yuan, and Y. Geng, "An improved grid-voltage feedforward strategy for high-power three-phase grid-connected inverters based on the simplified repetitive predictor," *IEEE Trans. Power Electron.*, vol. 31, no. 5, pp. 3880–3897, May 2016.

[4] V. Salis, A. Costabeber, S. M. Cox, P. Zanchetta, and A. Formentini, "Stability boundary analysis in single-phase grid-connected inverters with PLL by LTP theory," *IEEE Trans. Power Electron.*, vol. 33, no. 5, pp. 4023–4036, May 2018.

[5] Q. Qian, B. Zhang, Z. Ni, S. Xie, J. Xu, and K. Xu, "Circulating resonant current suppression for current-controlled inverters based on output impedance shaping," in *Proc. IEEE Energy Convers. Congr. Expo.*, 2017, pp. 4794–4798.

[6] S. Chi, L. Cheng, X. Li, and M. Hou, "A new suppression strategy for switching frequency circulating current in parallel inverters," in *Proc. 8th Renewable Power Gener. Conf.*, 2019, pp. 1–7.

[7] J. Liu, X. Qin, H. Lin, and L. Bu, "Analysis on circulating current of parallel inverter with SPWM modulation for AC motor drive," in *Proc. Int. Conf. Model., Identification, Control*, 2012, pp. 1080–1086.

[8] X. Wang and F. Blaabjerg, "Harmonic stability in power electronic-based power systems: Concept, modeling, and analysis," *IEEE Trans. Smart Grid*, vol. 10, no. 3, pp. 2858–2870, May 2019.

[9] S. Song, Z. Wei, Y. Lin, B. Liu, and H. Liu, "Impedance modeling and stability analysis of PV grid-connected inverter systems considering frequency coupling," *CSEE J. Power Energy Syst.*, vol. 6, no. 2, pp. 279–290, Jun. 2020.

[10] J. Sun, "Impedance-based stability criterion for grid-connected inverters," *IEEE Trans. Power Electron.*, vol. 26, no. 11, pp. 3075–3078, Nov. 2011.

[11] C. Yu et al., "Modeling and resonance analysis of multiparallel inverters system under asynchronous carriers conditions," *IEEE Trans. Power Electron.*, vol. 32, no. 4, pp. 3192–3205, Apr. 2017.

[12] Y. Cai, Y. He, H. Zhang, H. Zhou, and J. Liu, "Research on harmonic state-space modeling and calculation analysis of low-switching-frequency grid-connected inverter considering the impact of digitization," *IEEE Trans. Power Electron.*, vol. 38, no. 1, pp. 1003–1021, Jan. 2023.

[13] Y. Cai, Y. He, H. Zhang, H. Zhou, and J. Liu, "Integrated design of filter and controller parameters for low-switching-frequency grid-connected inverter based on harmonic state-space model," *IEEE Trans. Power Electron.*, vol. 38, no. 5, pp. 6455–6473, May 2023.

[14] M. Lu, Y. Yang, B. Johnson, and F. Blaabjerg, "An interaction-admittance model for multi-inverter grid-connected systems," *IEEE Trans. Power Electron.*, vol. 34, no. 8, pp. 7542–7557, Aug. 2019.

[15] Y. Wang, X. Wang, F. Blaabjerg, and Z. Chen, "Frequency scanning-based stability analysis method for grid-connected inverter system," in *Proc. IEEE 3rd Int. Future Energy Electron. Conf. ECCE Asia*, 2017, pp. 1575–1580.

[16] H.-C. Chen, P.-T. Cheng, X. Wang, and F. Blaabjerg, "A passivity-based stability analysis of the active damping technique in the offshore wind farm applications," *IEEE Trans. Ind. Appl.*, vol. 54, no. 5, pp. 5074–5082, Sep./Oct. 2018.

[17] X. Wang, F. Blaabjerg, and W. Wu, "Modeling and analysis of harmonic stability in an AC power-electronics-based power system," *IEEE Trans. Power Electron.*, vol. 29, no. 12, pp. 6421–6432, Dec. 2014.

[18] Q. Peng, G. Buticchi, N. M. L. Tan, S. Guenter, J. Yang, and P. Wheeler, "Modeling techniques and stability analysis tools for grid-connected converters," *IEEE Open J. Power Electron.*, vol. 3, pp. 450–467, Jul. 2022.

[19] Y. Song, S. Sahoo, Y. Yang, and F. Blaabjerg, "Quantitative mapping of modeling methods for stability validation in microgrids," *IEEE Open J. Power Electron.*, vol. 3, pp. 679–688, Oct. 2022.

[20] N. Pogaku, M. Prodanovic, and T. C. Green, "Modeling, analysis and testing of autonomous operation of an inverter-based microgrid," *IEEE Trans. Power Electron.*, vol. 22, no. 2, pp. 613–625, Mar. 2007.

[21] V. Purba, B. B. Johnson, M. Rodriguez, S. Jafarpour, F. Bullo, and S. V. Dhople, "Reduced-order aggregate model for parallel-connected single-phase inverters," *IEEE Trans. Energy Convers.*, vol. 34, no. 2, pp. 824–837, Jun. 2019.

[22] C. Chen, J.-S. Lai, D. Martin, and Y.-S. Lee, "State-space modeling, analysis, and implementation of paralleled inverters for microgrid applications," in *Proc. IEEE 25th Appl. Power Electron. Conf. Expo.*, 2010, pp. 619–626.

[23] Y. Wang, X. Wang, Z. Chen, and F. Blaabjerg, "State-space-based harmonic stability analysis for paralleled grid-connected inverters," in *Proc. 42nd Annu. Conf. IEEE Ind. Electron. Soc.*, 2016, pp. 7040–7045.

[24] C. Zhang, X. Li, X. Xing, B. Zhang, R. Zhang, and B. Duan, "Modeling and mitigation of resonance current for modified LCL-type parallel inverters with inverter-side current control," *IEEE Trans. Ind. Inform.*, vol. 18, no. 2, pp. 932–942, Feb. 2022.

[25] Y. Wang, X. Wang, F. Blaabjerg, and Z. Chen, "Harmonic resonance assessment of multiple paralleled grid-connected inverters system," in *Proc. IEEE 3rd Int. Future Energy Electron. Conf. ECCE Asia*, 2017, pp. 2070–2075.

[26] J. Kwon, X. Wang, F. Blaabjerg, C. L. Bak, A. R. Wood, and N. R. Watson, "Linearized modeling methods of AC–DC converters for an accurate frequency response," *IEEE J. Emerg. Sel. Topics Power Electron.*, vol. 5, no. 4, pp. 1526–1541, Dec. 2017.

[27] J. Zhang, X. Yang, W. Chen, H. Zhou, and J. Luo, "A multifrequency small-signal model for the MLCL-filtered grid-connected inverter considering the FCE of nonlinear inductors," *IEEE Trans. Ind. Electron.*, vol. 70, no. 5, pp. 4901–4911, May 2023.

[28] D. Yang, X. Wang, and F. Blaabjerg, "Sideband harmonic instability of paralleled inverters with asynchronous carriers," *IEEE Trans. Power Electron.*, vol. 33, no. 6, pp. 4571–4577, Jun. 2018.

[29] L. Wu, X. Ruan, Z. Lin, and H. Zhang, "Circulating current analysis of paralleled grid-connected inverters based on the multi-frequency model," in *Proc. IEEE Energy Convers. Congr. Expo.*, 2021, pp. 353–360.

[30] Z. Xu, B. Li, S. Wang, S. Zhang, and D. Xu, "Generalized single-phase harmonic state space modeling of the modular multilevel converter with zero-sequence voltage compensation," *IEEE Trans. Ind. Electron.*, vol. 66, no. 8, pp. 6416–6426, Aug. 2019.

[31] J. Kwon, X. Wang, C. L. Bak, and F. Blaabjerg, "Harmonic instability analysis of single-phase grid connected converter using harmonic state space (HSS) modeling method," in *Proc. IEEE Energy Convers. Congr. Expo.*, 2015, pp. 2421–2428.
[32] J. Kwon, X. Wang, F. Blaabjerg, C. L. Bak, V.-S. Sularea, and C. Busca, "Harmonic interaction analysis in a grid-connected converter using harmonic state-space (HSS) modeling," *IEEE Trans. Power Electron.*, vol. 32, no. 9, pp. 6823–6835, Sep. 2017.
[33] X. Chen, S. Yu, and X. Ge, "Modelling and stability analysis of virtual synchronous machine using harmonic state-space modelling method," *J. Eng.*, vol. 2019, no. 16, pp. 2597–2603, Dec. 2018.
[34] C. Gong, W. K. Sou, and C. S. Lam, "H∞ optimal control design of static var compensator coupling hybrid active power filter based on harmonic state-space modeling," *CPSS Trans. Power Electron. Appl.*, vol. 6, no. 3, pp. 227–234, Sep. 2021.
[35] J. Kwon, X. Wang, C. L. Bak, and F. Blaabjerg, "The modeling and harmonic coupling analysis of multiple-parallel connected inverter using harmonic state space (HSS)," in *Proc. IEEE Energy Convers. Congr. Expo.*, 2015, pp. 6231–6238.

Yuxi Cai (Student Member, IEEE) received the B.S. and M.S. degrees from Xi'an University of Technology, Xi'an, China, in 2016 and 2019, respectively, and the Ph.D. degree from Xi'an Jiaotong University, Xi'an, China, in 2023, all in electrical engineering.

She is currently a Researcher with Xi'an Research Institute of High-Tech, Xi'an, China. Her research interest focuses on the application of power electronics in power system.

Yingjie He (Senior Member, IEEE) received the B.S., M.S., and Ph.D. degrees in electrical engineering from Huazhong University of Science and Technology, Wuhan, China, in 1999, 2003, and 2007, respectively.

He was with the Power Electronics and Renewable Energy Center, Xi'an Jiaotong University (XJTU), Xi'an, China, as a Postdoctoral Researcher, and with Aalborg University, Aalborg, Denmark, as a Visiting Scholar. He is currently an Associate Professor and Doctoral Supervisor with XJTU. He has authored or coauthored more than 100 journal and conference papers, such as IEEE TRANSACTIONS ON POWER ELECTRONICS and IEEE TRANSACTIONS ON INDUSTRIAL ELECTRONICS. His research interests include multilevel converter and its control technology, application of power electronics in power system, power quality, and its control technology.

Dr. He was the recipient of the Second Prize of Science and Technology Progress from China Power Supply Society in 2021, the Science and Technology Progress Award from Shaanxi Power Supply Society in 2022, and the Special Contribution Award from Proceedings of the CSEE. He is selected as the High-level Talent of Shaanxi Power Supply Society and the High-level Talent of Zhenjiang, Jiangsu. He is an Executive Director of the IEEE Flexible AC Transmission Technology Subcommittee (China), an Executive Director of Shaanxi Power Supply Society, a Senior Member of China Electrotechnical Society, a Member of Power Quality Special Committee of China Power Supply Society, and an Appraisal Expert of National Natural Science Foundation and Ministry of Science and Technology of China.

Haoting Du (Student Member, IEEE) received the B.S. degree in electrical engineering from China Agricultural University, Beijing, China, in 2021. He is currently working toward the Ph.D. degree in electrical engineering with Xi'an Jiaotong University, Xi'an, China.

His research interest is modulation strategy of multilevel inverters.

Jinjun Liu (Fellow, IEEE) received the B.S. and Ph.D. degrees in electrical engineering from Xi'an Jiaotong University (XJTU), Xi'an, China, in 1992 and 1997, respectively.

He was a Faculty Member with the School of Electrical Engineering, XJTU. From late 1999 to early 2002, he was a Visiting Scholar with the Center for Power Electronics Systems, Virginia Polytechnic Institute and State University, Blacksburg, VA, USA. In late 2002, he was promoted to a Full Professor and then the Head of the Power Electronics and Renewable Energy Center, XJTU, which now comprises more than 20 faculty members and more than 200 graduate students and carries one of the leading power electronics programs in China. From 2005 to early 2010, he was an Associate Dean with the School of Electrical Engineering, XJTU, and from 2009 to early 2015, the Dean for Undergraduate Education of XJTU. He is currently an XJTU Distinguished Professor of power electronics. He coauthored 3 books (including 1 textbook), authored or coauthored more than 500 technical papers in peer-reviewed journals and conference proceedings, holds more than 50 invention patents (China/US/Europe), and delivered for many times plenary keynote speeches and tutorials at IEEE conferences or China national conferences in power electronics area. His research interests include modeling, control, and design methods for power converters and electronified power systems, power quality control and utility applications of power electronics, and microgrids for sustainable energy and distributed generation.

Dr. Liu was the recipient of eight times governmental awards at national level or provincial/ministerial level for scientific research/teaching achievements, the 2006 Delta Scholar Award, the 2014 Chang Jiang Scholar Award, the 2014 Outstanding Sci-Tech Worker of the Nation Award, the 2016 State Council Special Subsidy Award, the IEEE TRANSACTIONS ON POWER ELECTRONICS 2016 and 2021 Prize Paper Awards, and the Nomination Award for the Grand Prize of 2020 Bao Steel Outstanding Teacher Award. He was the IEEE Power Electronics Society Region 10 Liaison and then China Liaison for 10 years. Since 2006, he has been an Associate Editor for IEEE TRANSACTIONS ON POWER ELECTRONICS. From 2015 to 2019, he was the Executive Vice President, and from 2020 to 2021, he was the Vice President for Membership of IEEE PELS. He was on the Board of China Electrotechnical Society 2012–2020 and was elected the Vice President in 2013 and the Secretary General in 2018 of the CES Power Electronics Society. Since 2013, he has been the Vice President for International Affairs, China Power Supply Society (CPSS) and since 2016, the inaugural Editor-in-Chief for the *CPSS Transactions on Power Electronics and Applications*. Since 2013, he has been the Vice Chair of the Chinese National Steering Committee for College Electric Power Engineering Programs.